Strong wind characteristics and dynamic response of a long-span suspension bridge during a storm

Aksel Fenerci*, Ph.D. candidate, Department of Structural Engineering, Norwegian University of Science and Technology, Trondheim, Norway

Ole Øiseth, Ph.D., Department of Structural Engineering, Norwegian University of Science and Technology, Trondheim, Norway

Keywords: suspension bridge, wind-induced vibration, buffeting response, extra-tropical cyclone, field measurement, turbulence characteristics

Abstract

As Storm Tor struck the western coast of Norway, wind speeds and bridge deck accelerations along the Hardanger Bridge girder were recorded by the monitoring system installed on the bridge. Using 13.5 hours of data, mean wind speed, turbulence intensities, gust factor, turbulence length scales, angle-of-attack, and one-point and two-point turbulence spectra are studied using 10-minute stationary averaging intervals. Using the measured turbulence statistics as inputs, the buffeting response of the bridge deck is calculated in the frequency domain. The calculated response is compared with the measured response in terms of the root-mean-square (RMS) of acceleration and displacement components and the power spectral density of the acceleration response. Significant discrepancies are found in the case of the vertical response. Predicting the spectral response is found to be more difficult than predicting the RMS response, in particular for high-frequency responses. Considering the spanwise non-uniformity of turbulence statistics did not affect the predictions significantly.

1. Introduction

In Norway, Coastal Highway E39 lies along the western coast and connects Trondheim to Kristiansand in southern Norway, eventually reaching Aalborg in Denmark. Today, a drive on the 1100 km highway from Trondheim to Kristiansand is interrupted by seven ferries, which results in a travel time of approximately 21 hours. The western coast is the most economically active region of Norway, where the majority of export goods are transported along the E39 route. Therefore, it is desirable to decrease travel time by replacing the ferry connections with bridges or subsea tunnels. This would involve crossing seven fjords ranging between 1500 and 5000 meters wide and between 600 and 1500 meters deep; for this purpose, bridges of unmatched scale would have to be built. Feasibility studies concerning such large scale bridge projects are being conducted by the Norwegian Public Roads Administration (NPRA) (Ellevset and Skorpa 2011). The focus is mainly given to the largest crossings (Sognefjørden 3.7 km, Bjørnafjørden 5 km). Different bridge concepts such as super long-span suspension bridges, multi-span suspension bridges with floating towers and pontoon bridges are being considered for the crossings. As the global demand for longer span cable-supported bridges grows, design of such structures against wind effects becomes increasingly important.

Field measurements of mean wind speed and turbulence are indispensable in characterization of the wind turbulence field for design of long-span bridges against gusty wind action. Owing to the increasing number of measurement campaigns (Brownjohn et al. 1994; Cao et al. 2009; Cheynet et al. 2016; Choi 1978; Cross et al. 2013; Hui et al. 2009a; b; Macdonald 2003; Miyata et al. 2002; Wang et al. 2017) and structural health monitoring projects with wind measurements (Wang et al. 2009, 2011, 2013, 2014; Xu 2013) around the world, more and more data on wind turbulence characteristics have been presented by researchers (Harstveit 1996; He et al. 2013; Hu and Ou 2013; Li et al. 2015; Peng et al. 2013). Such works provide valuable information on the general characteristics of the wind field (stationarity, homogeneity, and one-point and two-point statistics) at specific sites. Information regarding site-

* Corresponding author: aksel.fenerci@ntnu.no

specific features, terrain effects and variability of the wind field are also beneficial in understanding the nature of gust loading on such structures (Pagnini and Solari 2002; Solari and Piccardo 2001). However, most of the listed studies concentrate on the Asia and Pacific with a focus on typhoon winds. Therefore, more data on the strong wind characteristics of European windstorms from relevant sites, such as Norwegian fjords, are required.

Stochastic dynamic analysis of wind-induced vibrations of cable-supported bridges was first introduced by Davenport (1962) and then improved by Scanlan (1978) with the introduction of flutter derivatives in the description of self-excited forces (Scanlan and Tomko 1971). Today, a multimode coupled approach (Chen et al. 2001; Jain et al. 1996; Katsuchi et al. 1998; Øiseth et al. 2010; Xu et al. 2000) is commonly used, where analysis may be conducted in either the frequency or time domain. Analyses considering skew-winds (Kimura and Tanaka 1992; Wang et al. 2011; Xie et al. 1991; Xu et al. 2003; Xu and Zhu 2005a; Zhu and Xu 2005), full-bridge models (Xu et al. 2000) and spanwise non-uniform winds (Hu et al. 2017) were conducted by researchers. In recent years, non-stationary wind models have also been adopted by many (Chen et al. 2007; Chen 2015; Hu et al. 2013, 2017; McCullough et al. 2014; Tao et al. 2017; Wang et al. 2016; Xu and Chen 2004). Despite analytical efforts, few attempts have been made toward validation of these methods using full-scale measurements (Bietry et al. 1995; Cheynet et al. 2016; Macdonald 2003; Park et al. 2012; Wang et al. 2011, 2013; Xu and Zhu 2005b). Although satisfactory predictions were obtained by some, significant discrepancies were also observed, especially in the case of complex terrain, where the wind is variable, nonstationary and not homogenous. Moreover, the amount of data used for comparison is in general limited, especially under strong winds. Clearly, more comparisons, preferably from strong wind recordings, are needed for a better understanding of the limits of such analyses and the uncertainty involved, as well as the sources of uncertainty.

This paper concentrates on the strong wind characteristics and dynamic response of the Hardanger Bridge during a storm event. General information on wind conditions at the site and the bridge response were addressed in Fenerci et al. (2017), Fenerci and Øiseth (2017) and Fenerci and Øiseth (2016a; b). The wind speeds and accelerations at several locations along the bridge deck were measured by a dense sensor network. The wind turbulence statistics during the storm are presented using 10-sminute averaging intervals. Using the measured turbulence statistics, the wind field along the bridge is modeled separately for each interval, and the dynamic response is calculated accordingly. The measured and calculated dynamic responses are then compared, and the results are discussed.

2. Hardanger Bridge and the monitoring system

The Hardanger Bridge (HB) is currently the longest suspension bridge in Norway with a single span of 1308 meters (Fig. 1). It is located in mountainous terrain in Norwegian fjords and is subjected to strong European windstorms. The unique wind exposure of the site and the slender deck of the bridge make it an attractive case study when investigating the wind-induced dynamic response of long-span suspension bridges in such complex terrain. For this reason, shortly after the bridge was opened to the public in 2013, it was instrumented by a state-of-the-art monitoring system to measure wind velocities and accelerations along the girder. The system is comprised of 20 accelerations and 9 anemometers, where the data is transferred on the bridge by Wi-Fi and synced by GPS time. The sensor layout is shown in Fig. 2**,** and the coordinates of each sensor are listed in Table 1, where the origin of the coordinate system was taken as the midspan of the bridge. Detailed information on the HB and the workings of the monitoring system can be found in Fenerci and Øiseth (2017).

Fig. 1. Panoramic view of the Hardanger Bridge toward the west (photograph by Aksel Fenerci/NTNU)

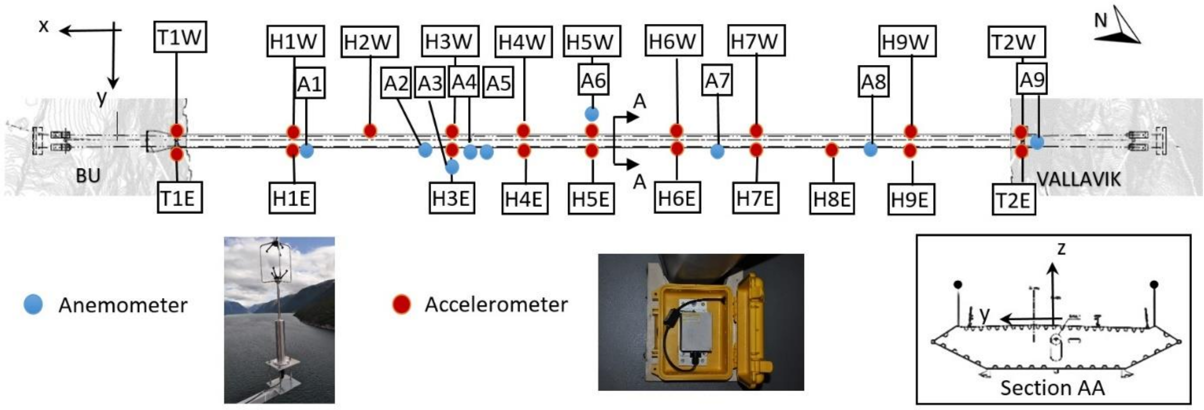

Fig. 2. The sensor layout

Table 1
Sensor names and coordinates

Wind sensors				Accelerometers			
Name	x (m)	y (m)	z (m)	Name	x (m)	y (m)	z (m)
A1	460	7.25	0.3	H1E/H1W	480	6.33/-6.64	-8.38
A2	280	7.25	3.2	H2W	360	-6.64	-6.41
A3	240	7.25	3.9	H3E/H3W	240	6.33/-6.64	-4.45
A4	200	7.25	4.6	H4E/H4W	120	6.33/-6.64	-2.48
A5	180	7.25	4.9	H5E/H5W	-7	6.33/-6.64	-0.4
A6	-10	-7.25	8	H6E/H6W	-120	6.33/-6.64	-2.25
A7	-180	7.25	5.2	H7E/H7W	-240	6.33/-6.64	-4.22
A8	-420	7.25	1.2	H8E	-360	6.33	-6.18
A9	-655	4.5	140	H9E/H9W	-480	6.33/-6.64	-8.15
				T1E/T1W	655	4.5/-4.5	120.5
				T2E/T2W	-655	4.5/-4.5	120.5

3. Storm Tor

On 29-30th January 2016, a European windstorm struck the coastline of Norway, Scotland and northern parts of Ireland and England. The extratropical cyclone was named and referred to as “Storm Tor” by the Norwegian Meteorological Institute, “Storm Gertrude” by the UK Met Office and Met Eirann of Ireland and “Storm Marita” by the Free University of Berlin in Germany. It will be referred to as “Storm Tor” here, adopting the Norwegian name. This severe storm affected several regions along the Norwegian coast, such as Sør-Trondelag, Møre og Romsdal, Sogn og Fjordane and also Hordaland, where the HB is located. The highest mean wind speed recorded during the storm was 48.9 m/s in a 10-minute averaging interval, and the highest measured gust was 61.7 m/s, both of which were recorded at a height of 75 m above ground at the Kråkenes Lighthouse in Møre og Romsdal. This was the highest wind speed officially recorded in Norway (Kristiansen et al. 2016). A public report by the Norwegian Meteoroligical Institute (2016) reported significant property damage (≈ 450 million NOK). Many regions were without power during the storm. The passage of the storm through the HB site has been successfully recorded by the HB monitoring system. The bridge was closed to traffic during most of the storm. Mean wind speeds of up to 30 m/s and wind gusts of up to 37 m/s were measured by the anemometers on the bridge, which were the highest recorded, during the first four-year period of the measurement campaign. Strong winds were recorded on both the 29th and 30th of January. However, in the rest of the paper, a continuous 13.5 hour period will be considered from 29th January at 12:00 (UTC time) until 30th January 1.30, where the highest wind speeds were recorded.

4. Wind turbulence characteristics

4.1. General

The wind velocity data acquired through eight anemometers (A1-A8) located at the HB deck were used to study the wind characteristics of Storm Tor. All anemometers are attached to the hangers of the bridge at a height of 8 meters from the bridge girder to avoid the disturbance of the wind flow due to the bridge deck. It should be noted that the z-coordinates of the anemometers are not the same due to the curvature of the bridge. The wind data were initially sampled at 32 Hz in polar coordinates and then downsampled to 20 Hz to have a common sampling rate with the acceleration data. When studying wind turbulence characteristics relevant to the dynamic response of land-based structures, it is customary to decompose the wind speed to its mean and fluctuating components, considering a certain averaging interval. Depending on the region and nature of the wind, an averaging interval between 1 minute and 1 hour is generally adopted, where the wind flow is considered sufficiently stationary. Defining a new coordinate system aligned in the direction of the mean wind speed (U), three orthogonal fluctuating wind components, namely, the along-wind (u), cross-wind (v) and vertical (w) turbulences are defined. The three turbulence components are then assumed as zero-mean stationary Gaussian random processes.

It is important that these assumptions be reasonably valid since the classical methods of wind induced response analysis of structures rely on these assumptions. Methods such as the run test or the reverse arrangement test (Bendat and Piersol 2000) were previously used on wind records to assess their stationarity (Cao et al. 2009, 2015; Tao et al. 2017). However, such methods provide an evaluation of randomness rather than stationarity and can be effective in highlighting underlying trends in wind records. A run test, following the work of Cao et al. (2015), was employed to assess the stationarity of 10-minute wind time series (U (t) + u (t)) obtained from the eight anemometers along the HB span, and the results are shown in Fig. 3. The majority of the recordings failed the test at a 5% significance level using 30 segments per signal, and no reasonable pattern of nonstationarity could be extracted. It is also observed that the test is highly dependent on the segment size and does not provide objective means for evaluation of stationarity. Recent studies (Chen et al. 2007; Tao et al. 2017; Wang et al. 2016) also showed that when there is no abrupt change in the wind direction or speed in the considered averaging interval, the wind statistics obtained with stationary and nonstationary models do not vary significantly. It has been reported that the discrepancy is high in length scales and very low-frequency part of the along-wind turbulence spectra because these are sensitive to the slowly varying mean speed. It should be noted that such discrepancies are not important for the wind field model adopted here. Also, experience suggests that a 10-min averaging interval is appropriate to minimize such slowly varying components. Therefore, owing to its extensive use in practice and wind-resistant design codes, the traditional stationary wind model will be used in this study. Quantification of the uncertainty introduced by the nonstationarity of the wind time series on the wind statistics and response prediction requires a nonstationary analysis, which is considered out of scope for this paper, where the aim is to evaluate the performance of state-of-the-art methods.

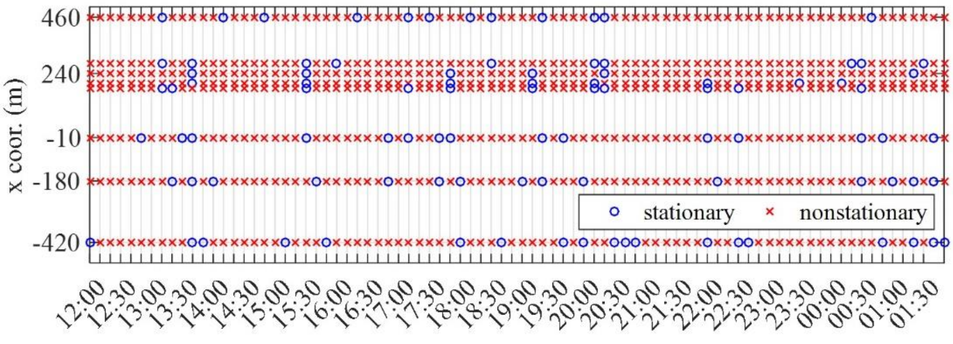

Fig. 3. Stationarity test on 10-minute recordings

Probability distributions of turbulence components for a 10-minute recording are plotted along with a normal distribution fit to demonstrate the normality of the data (Fig. 4**)**. It is seen that the distributions of u and w components agree reasonably well with the Gaussian distribution, where the v component does not, presumably due to the effect of the mountains on either side of the bridge.

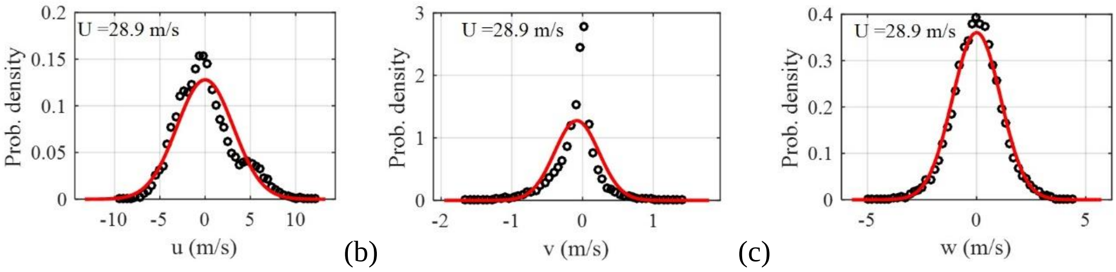

Fig. 4. Probability distributions of turbulence components for a 10-minute recording recoded on 29/01/2016 between 18:40 and 18:50: (a) along-wind, (b) cross-wind and (c) vertical components

4.2. Mean wind speed and direction

The 10-minute mean wind speed during the storm is plotted in Fig. 5 using the data from the midspan sensor (A6). As is easily observed from the plot, the wind speed rapidly increased in the beginning of the storm and reached 20 m/s around 13.00. The strong winds were sustained until 23.00, where the wind speed decreased to approximately 10 m/s suddenly. In this ten-hour period, the wind speed was generally in the 20-25 m/s range, except for the one hour period between 18.00 and 19.00, where it reached its peak of approximately 30 m/s. Including the built-up phase and the end of the storm, a total of 13.5 hours of well-acquired data are considered to study the storm. The mean wind speed data are also plotted in Fig. 6 in a wind rose on the topographical map of the region to show the direction of the wind and the upwind topographical conditions. As shown in the figure, the storm winds were nearly perpendicular to the bridge longitudinal axis, where the wind direction was sustained during the storm. A contour plot was also generated using the data from all sensors to show the variation of the wind speed along the bridge span **(**Fig. 7). The data points are highlighted in the plot, where the contour was obtained using linear interpolation between points. In general, higher mean wind speeds were measured toward the south end of the bridge during the storm. Finally, the time histories of wind directions shown in Fig. 8 are plotted for three anemometers: one at the midspan (A6) and two at either end of the bridge span (A1 & A8). It is seen that the wind direction measured at A1 and A8 were very close to each other, where slightly more skewed winds were measured at the midspan sensor.

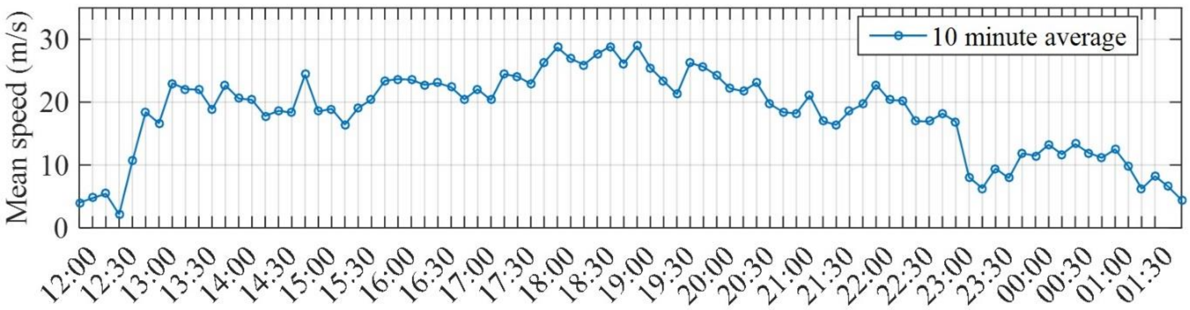

Fig. 5. Mean wind speed at the midspan (sensor A6)

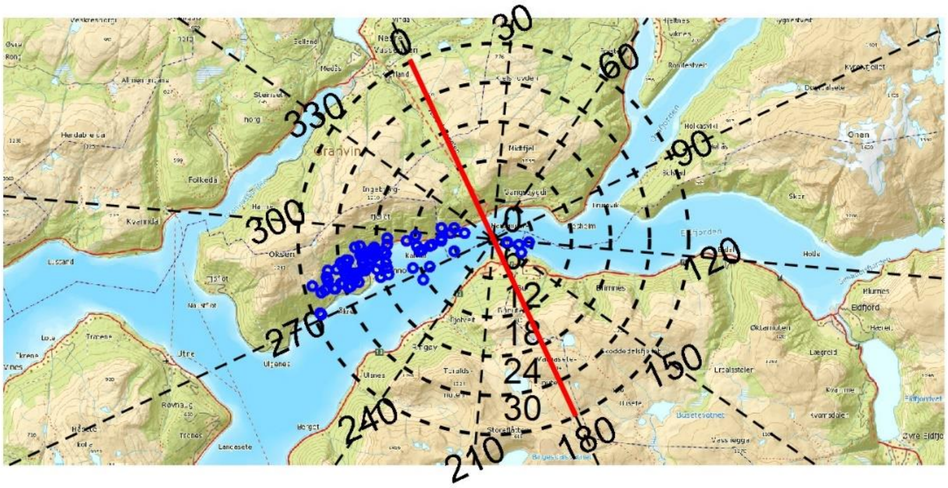

Fig. 6. Wind rose plot of 10-minute mean wind speed at the midspan (m/s) (base map courtesy of ©Kartverket, www.kartverket.no)

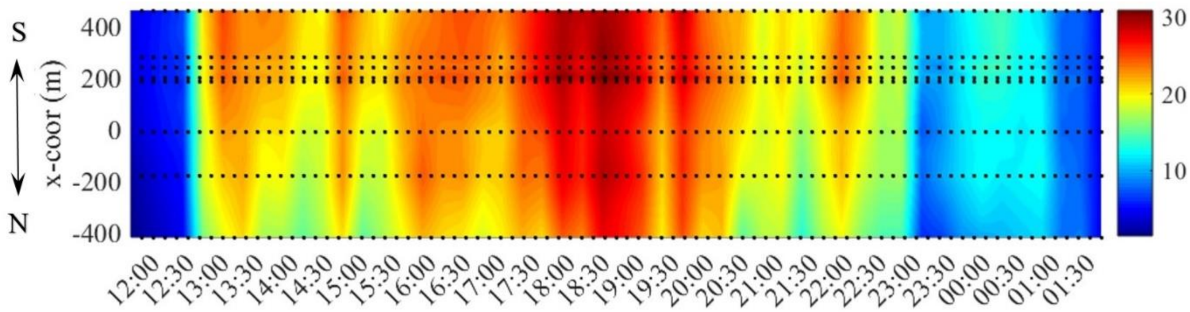

Fig. 7. Contour plot of mean wind speed

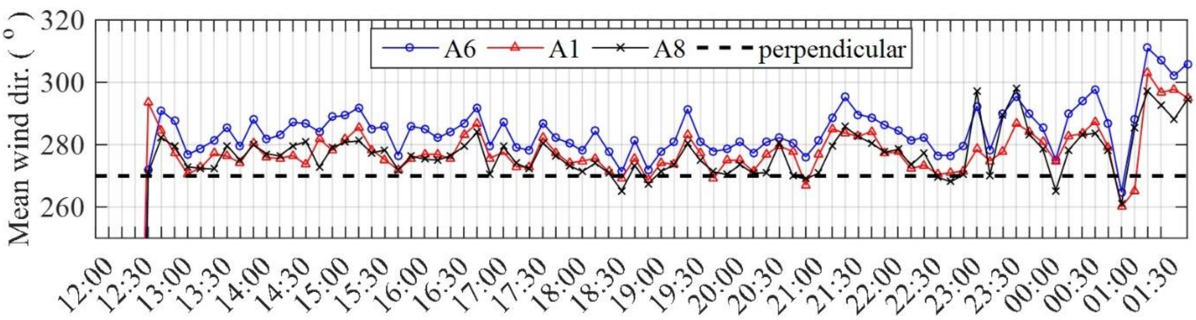

Fig. 8. Mean wind direction from anemometers A1, A6 and A8

4.3. Gust wind speed and gust factor

The gust wind speed is obtained by averaging the wind speed in a much shorter interval than the mean wind speed and is used to represent sudden changes in wind speed (gusts), which are more closely related to the dynamic response of structures (Cao et al. 2015; Holmes 2007; Krayer and Marshall 1992; Kwon and Kareem 2014; Shu et al. 2015). Typically, a gust averaging interval of 2-3 seconds is adopted to estimate the highest instantaneous wind speed. A gust factor is also commonly used to convert mean wind speed to gust wind speed, especially in the design of structures subjected to gusty winds. It can be written as

$$G_u = \frac{|u_t|_{\max}}{U_T} \tag{1}$$

where u_t is the gust speed averaged over gust interval t and U_T is the mean wind speed with averaging interval T. The gust wind speed and the gust factor for the 10-minute recordings of Storm Tor were calculated using a 3-second gust averaging interval and presented in Fig. 9. In the figure, a running 10-minute mean wind speed is also plotted on top of the gust speed to show the evolution of the 10-min mean wind speed. The maximum gust speed was around 37 m/s. The gust factor at the midspan is given in Fig. 10a. The gust factor seems sensitive to the stationarity of the signal. Typically, high gust factors were obtained when the wind speed or direction was changing rapidly; i.e., there is a profound trend in the time series. Discarding those, the gust factor was around 1.3-1.5 during the storm. A contour plot of the gust factor is also presented in Fig. 10b. The gust factor was in general larger at the north end of the bridge.

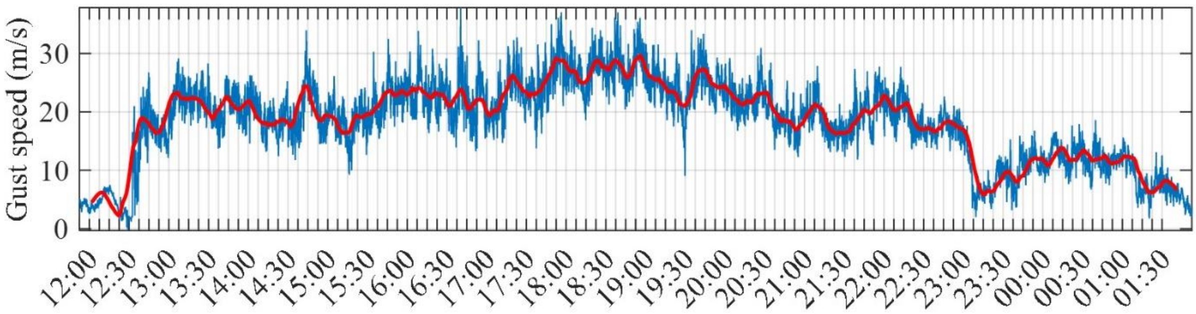

Fig. 9. Gust wind speed with 10-minute moving mean wind speed at the midspan (sensor A6)

(a)

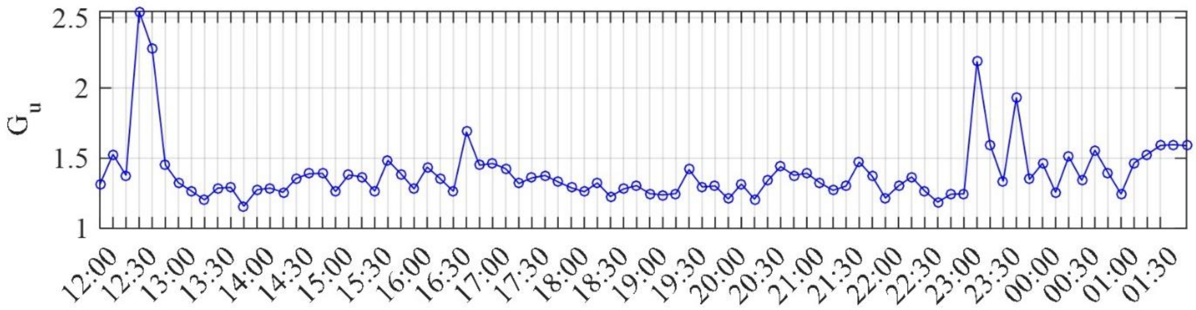

(b)

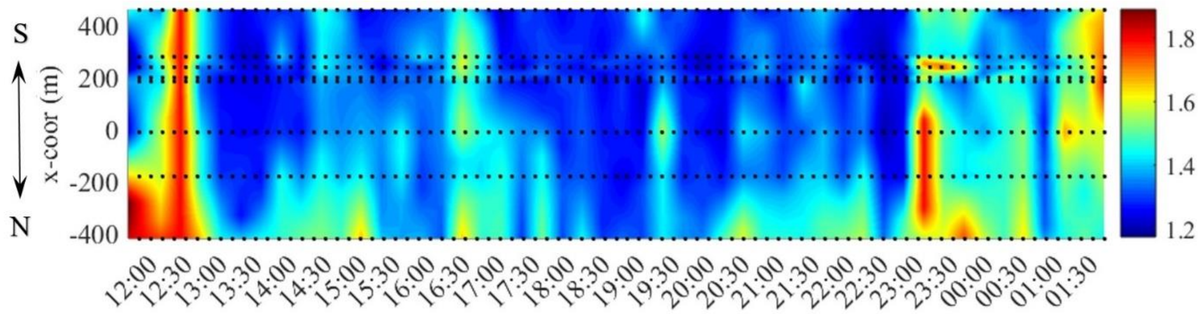

Fig. 10. Gust factor (a) at the midspan and (b) contour plot

4.4. Turbulence intensity

Turbulence intensity is the ratio of the standard deviation of the turbulence components (σ_u, σ_v, σ_w) to the mean wind velocity (U), and it is of vital importance in predicting the dynamic response since it is a direct measure of the energy content of turbulence. Turbulence intensities for the three turbulence components (I_u, I_v, I_w) are given in Fig. 11a for the midspan and Fig. 11b-d for all sensors using contour plots. Similar to the gust factor, high turbulence intensities were associated with the non-stationary signals. During the sustained part of the storm, along-wind turbulence intensity (I_u) varied between 10-20%, and vertical turbulence intensity (I_w) varied between 4-6%. Cross-wind turbulence intensity (I_v) was around 2%. The contour plots of turbulence intensities show a similar pattern to the gust factor (Fig. 10), with higher values toward the north. The ratio I_u:I_v:I_w between the turbulence intensities is calculated as 1:0.14:0.4 using the mean values (0.125:0.018:0.051). Only recordings above 15 m/s were considered not to include the severely non-stationary recordings. The relation between turbulence intensity and gust factor is given in Fig. 12 along with two empirical models (Choi 1983; Ishizaki 1983). The correlation between two statistical parameters are apparent, and the model by Ishizaki (1983) gives a good approximation of the data for this particular storm.

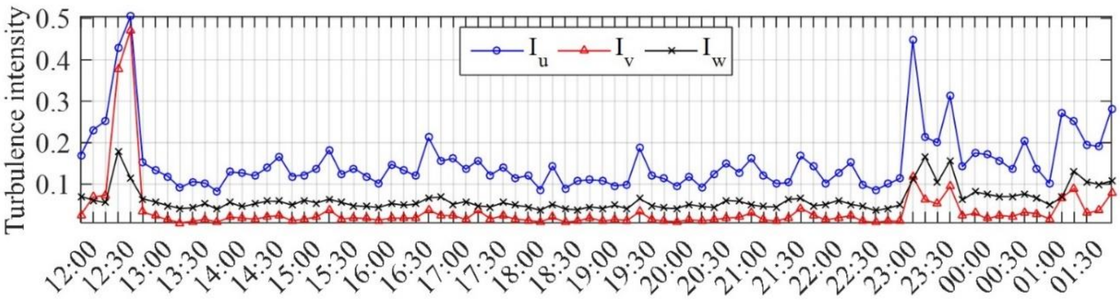

(a)

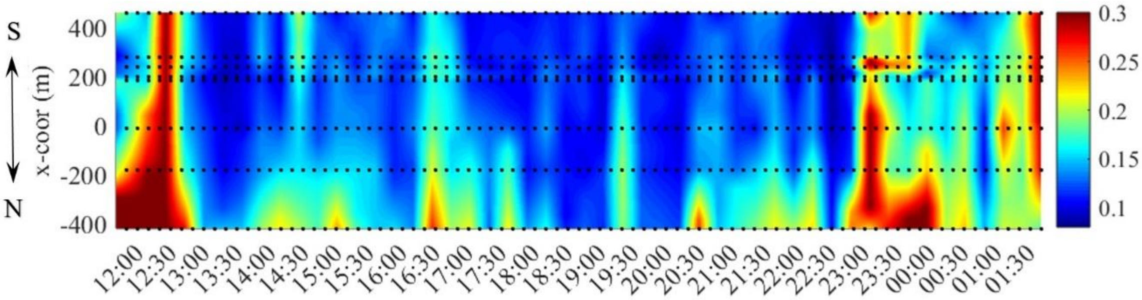

(b)

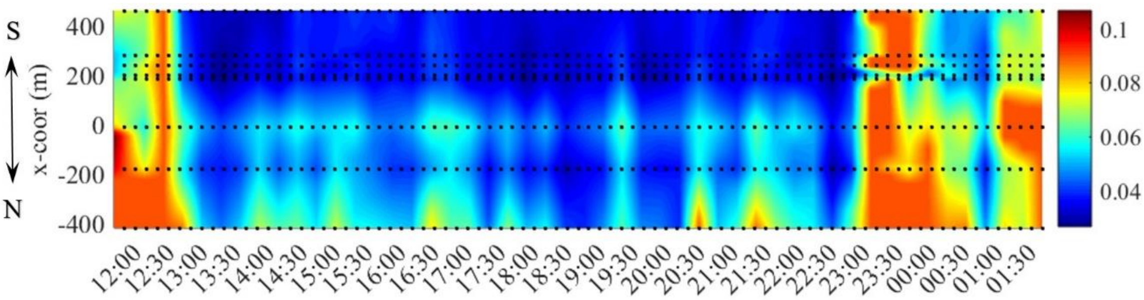

(c)

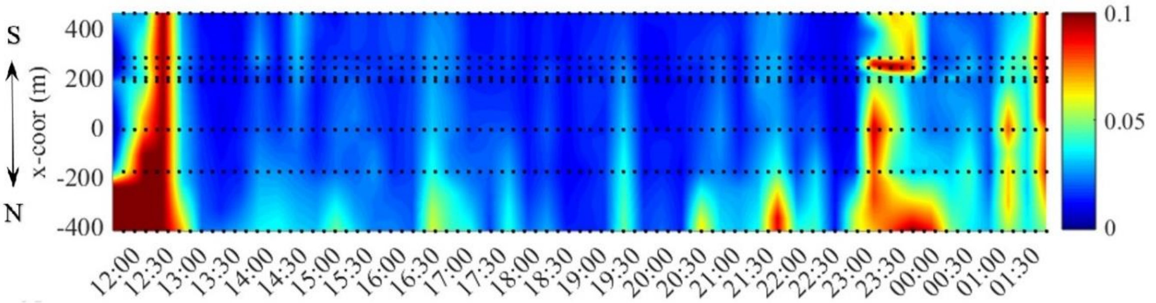

(d)

Fig. 11. Turbulence intensity (a) at the midspan and contour plots: (b) I_u (c) I_v (d) I_w

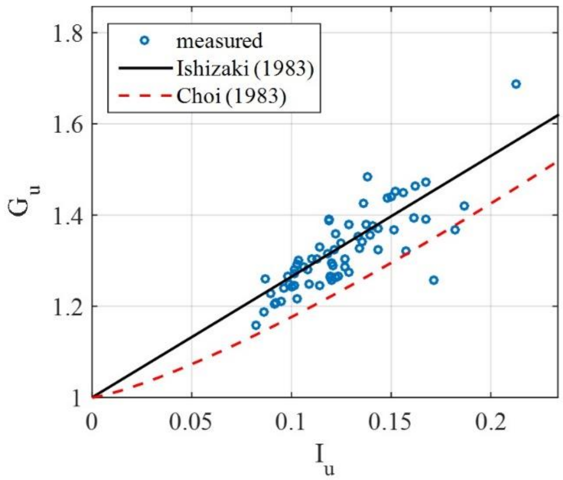

Fig. 12. Gust factor vs. along-wind turbulence intensity at the midspan

4.5. Cross-correlation of u-w turbulence

The one-point correlation of the u and w turbulence components is assessed through the cross correlation coefficient, given as

$$\gamma_{uw} = \frac{\sigma_{uw}}{\sqrt{\sigma_u \sigma_w}}, \quad \sigma_{uw} = \frac{1}{N-1}\sum_{i=1}^{N}(u_i - \mu_u)*(w_i - \mu_w) \tag{2}$$

where σ_{uw} denotes the cross-covariance of the turbulence components and σ_u, σ_w are the standard deviations. The cross-correlation coefficient will then assume a value between -1 and 1, and it relates to the vertical shear or energy loss of turbulence due to ground roughness. The cross-correlation coefficient of u and w components were calculated for all recordings, and they are presented in Fig. 13. It is observed that the correlation between the u and w components was in general positive, contradicting the theoretical consideration in flat homogenous terrain and the neutral boundary layer. The average cross-correlation coefficient was 0.067, where the corresponding cross-covariance was 0.17.

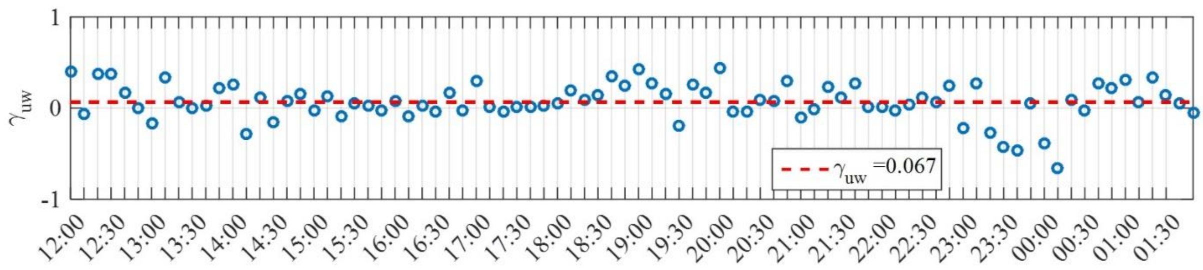

Fig. 13. Cross-correlation coefficient of u and w turbulence components at the midspan

4.6. Turbulence length scale

The length scales of turbulence are the average length of turbulent eddies and hence give valuable information on the spectral content of the turbulence components. In the along-wind direction, three turbulence length scales (L_u, L_v, L_w) can be defined. If Taylor's hypothesis of frozen turbulence is assumed valid, the length scales in the along-wind direction can be estimated using the time auto-correlation of the turbulence components. The three length scales were calculated for the 10-minute recordings using the midspan sensor, and they are presented in Fig. 14 with recommendations of ESDU (2001) and N400 (Norwegian bridge design handbook, Statens-Vegvesen 2009). The estimated length scales show immense variability between 10-minute recordings of the same storm, especially for the along-wind component, and the recommended values both by N400 (178:44:15 m) and ESDU (240:20:20 m) were in general much smaller compared to the calculated values. In this case, it should also be noted that since low frequency components in the turbulence recordings are of utmost importance in the calculation of the length scales, results are very sensitive to the signal stationarity and trends in the data. Since none of the recorded signals is strictly stationary, generally high values are obtained from measurements, with significant variability. This was also observed in the work of Tao et al. (2017), where a nonstationary analysis was carried out. Using average values, the L_u:L_v:L_w ratio was around 1:0.3:0.2 (539:168:104 meters). Consequently, for the terrain in consideration, the use of length scales with the stationary wind model should be avoided when possible due to the randomness in field data and its sensitivity to signal stationarity.

(a)

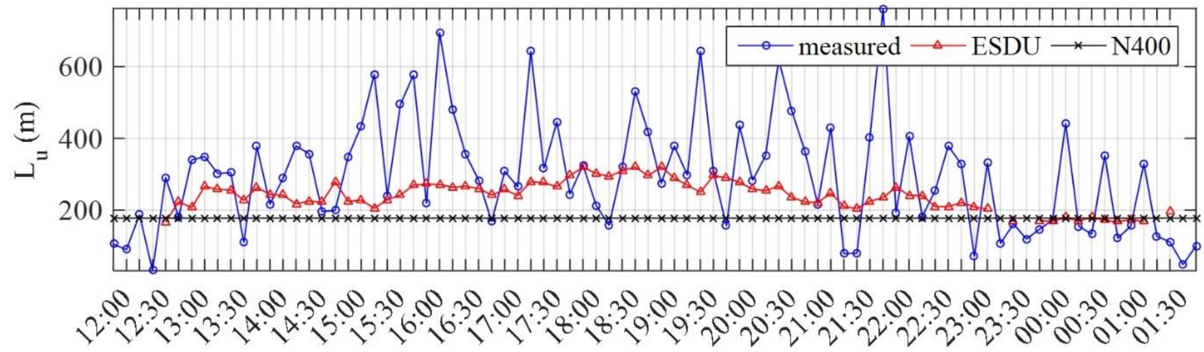

(b)

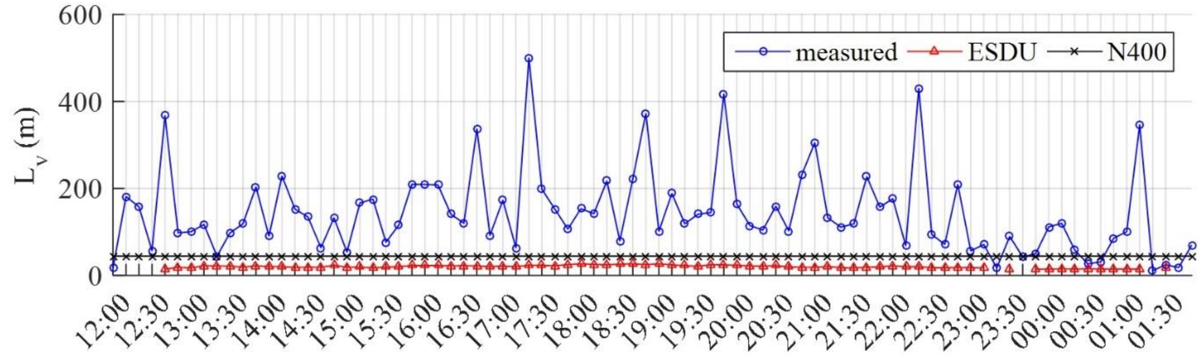

(c)

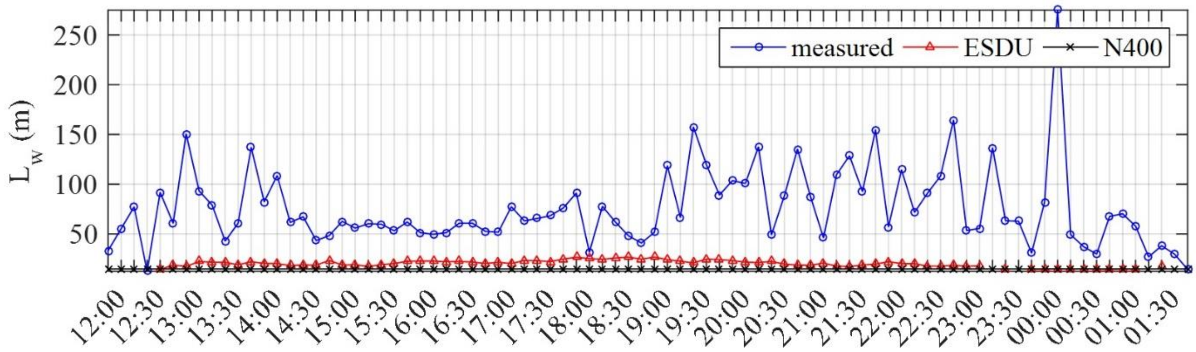

Fig. 14. Turbulence length scales: (a) along-wind (b) cross-wind and (c) vertical components

Since a one-hour averaging interval is also commonly used in the calculation of length scales, one-hour length scales were also calculated for the sake of comparison. Considering only the strong wind part of the storm, length scales of 1900 meters and 138 meters were obtained in average for the along-wind and vertical turbulences, respectively. It is seen that the vertical length scales were more or less the same, but the along-wind length scales increased even more, where the variability in results persisted. This is due to the sensitivity of the auto-correlation function to the low-frequency components in the signals. Consequently, if there are slowly varying trends in the mean wind speed; it appears as a low-frequency correlation in the auto-correlation function, resulting into high estimates of the along-wind integral length scale. The difference can easily be observed in Fig. 15, where the autocorrelation function estimate for a 1-hour recording is compared with the average of estimates for 10-minute segments. It is apparent that the auto-correlation function is much higher for the longer recording, due to nonstationary components in the signal and this is consistent throughout the storm.

(a)

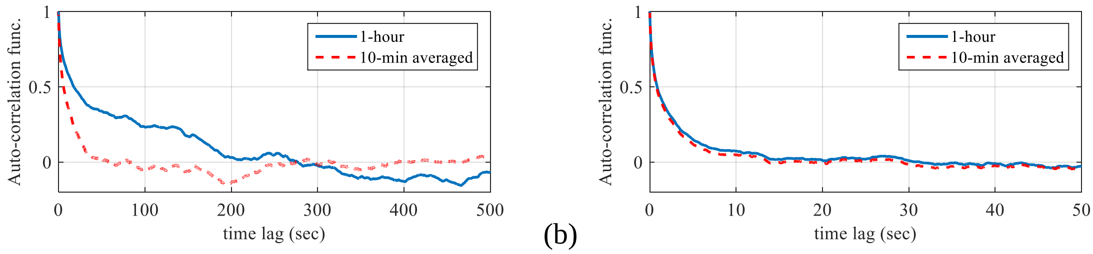

Fig. 15. The effect of averaging interval on the auto-correlation functions: (a) along-wind and (b) vertical turbulence

4.7. Angle-of-attack

The angle-of-attack is defined here as the angle between the mean wind velocity vector and the horizontal plane. For the 10-minute recordings, the angle-of-attack was calculated using the midspan anemometer data, and the results are presented in Fig. 16. It is seen that the wind velocity vector was consistently inclined around 2.5° upwards on average during the whole storm.

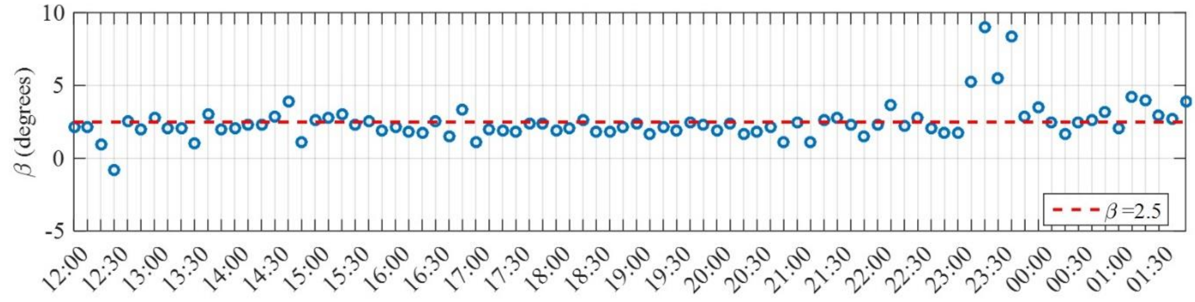

Fig. 16. The angle-of-attack

4.8. One-point spectra of turbulence

In wind-induced dynamic response prediction of long-span cable-supported bridges, the buffeting load on the structure is generally described by a cross-spectral density matrix, including one-point and two-point statistics of the along-wind and vertical turbulence components. Therefore, a good representation of spectral characteristics of turbulence is crucial for accurate response prediction. The one-point auto and cross spectra of the u and w components at the midspan were calculated for all recordings above a mean wind speed of 15 m/s using Welch's (1967) averaged periodogram method with eight segments and 50% overlap. The spectra are shown in Fig. 17. The scatter in the data can immediately be observed despite the averaging of the periodogram estimates. The average spectra of all recordings are also shown in Fig. 17, along with several analytical spectra given by Kaimal et al. (1972), von Karman (1948), ESDU (2001) and N400 (Statens-Vegvesen 2009). It is seen that in the average sense, the analytical spectra were not successful in matching the measurement data, except for the von Karman u-spectrum.

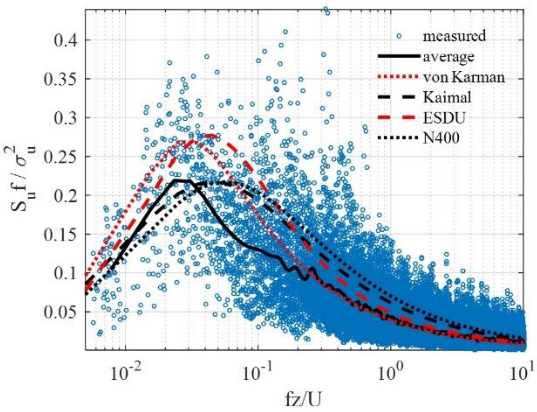

(a)

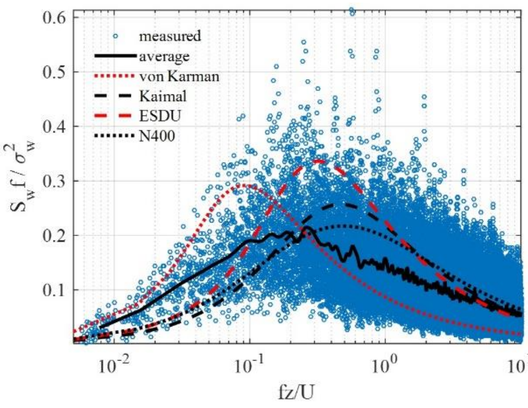

(b)

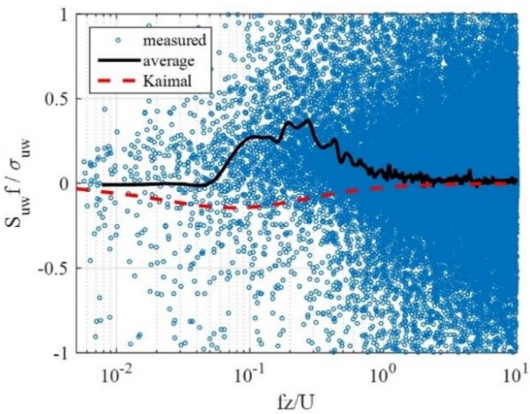

(c)

Fig. 17. One-point spectra of turbulence at the midspan: (a) auto-spectra of along-wind turbulence, (b) auto-spectra of vertical turbulence and (c) cross-spectra of along-wind and vertical turbulences

The turbulence spectra were also estimated using a one-hour averaging interval. In this case, six segments with 75% overlap was used to average the periodogram estimates. This resulted in an increased frequency resolution of 0.0003052 Hz. In return, the estimates have larger variance due to lower number of averaged segments. The estimates are shown in Fig. 18. It is seen that the vertical turbulence spectra remained almost unchanged, where the peak of the along-wind turbulence spectra was moved to lower frequencies. This also roots from the fact that the signals are nonstationary and accommodate slowly varying trends. Nevertheless, it should be stressed again that the wind field model used here will not be affected greatly from such trends since it is not strongly dependent on the length scale estimates or the very low-frequency part of the turbulence spectra.

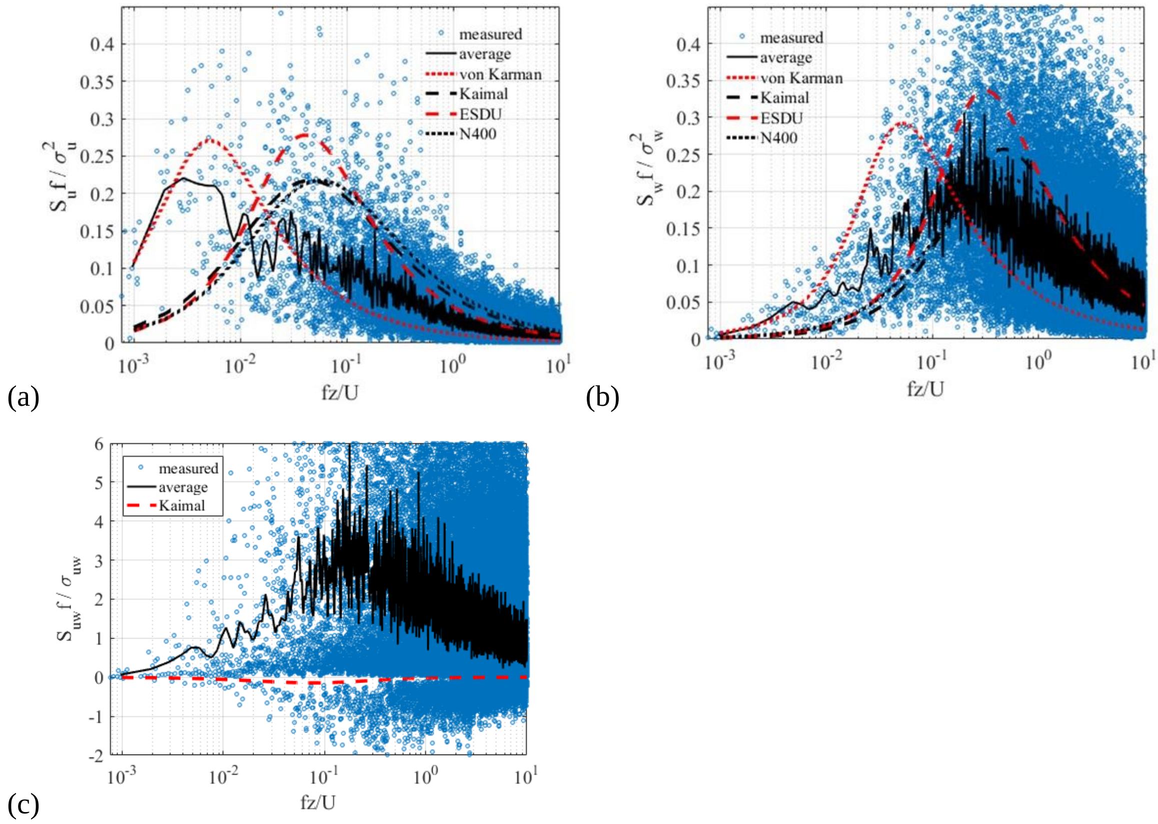

Fig. 18. One-point spectra of turbulence at the midspan using a one-hour averaging interval: (a) auto-spectra of along-wind turbulence, (b) auto-spectra of vertical turbulence and (c) cross-spectra of along-wind and vertical turbulences

The measurement data also accommodate significant variability, making it difficult to deduce a single spectral expression for the entire storm. Therefore, a Kaimal-type expression (Kaimal et al. 1972; Solari and Piccardo 2001) was fitted in the least-squares sense to the estimated 10-min spectra. The parametric spectral formula is written as

$$\frac{S_{u,w} f}{\sigma_{u,w}{}^2} = \frac{A_{u,w} f_z}{(1+1.5A_{u,w} f_z)^{5/3}}, \quad f_z = \frac{fz}{U} \tag{3}$$

where $A_{u,w}$ are the parameters to be fitted. In the expression, $S_{u,w}$ denote the auto-spectral densities, f denotes frequency in Hz and z denotes the height above ground (68 m for the midspan). An example fit is demonstrated in Fig. 19 with its 99% confidence intervals for a 10-min recording with 29 m/s mean wind velocity. The root-mean-square error (RMSE) values giving the standard error of the fit are also indicated in the figure. From visual observations and RMSE values, it can be stated that the fitted curves give a reasonable approximation of the measured spectra. It should be noted that the fit is made only for the part of the spectra up to 1 Hz, which is considered the important frequency range for dynamic response calculations; however, reasonable agreement with the data is observed also in the higher frequency range.

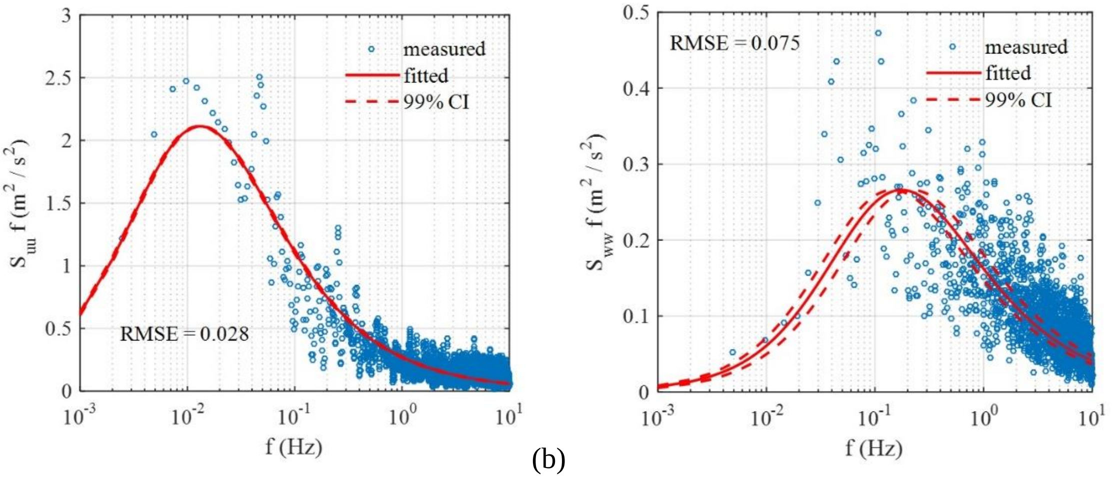

(a) (b)

Fig. 19. Fitting of the one-point spectra using Eqn. (3) using a 10-minute recording recoded on 29/01/2016 between 18:40 and 18:50. (A_u = 32.3, A_w = 2.42, RMSE = root-mean-squared-error, CI = confidence interval) (a) auto-spectra of along-wind turbulence, (b) auto-spectra of vertical turbulence

The spectral parameters $A_{u,w}$ were then calculated for all 10-minute recordings. The results are presented for the midspan sensor in Fig. 20 and as contour plots in Fig. 21. 99% confidence intervals for the parameters are also shown in the figures using error bars. It is seen that the parameters showed variation between 10-minute recordings during the storm. The average values, which are also shown on the plots, were quite similar to the values of the Kaimal spectra. The parameter A_w was relatively more stable compared to A_u during the storm. The A_u was in general higher toward the south side, where A_w was consistently higher at the midspan of the bridge.

(a)

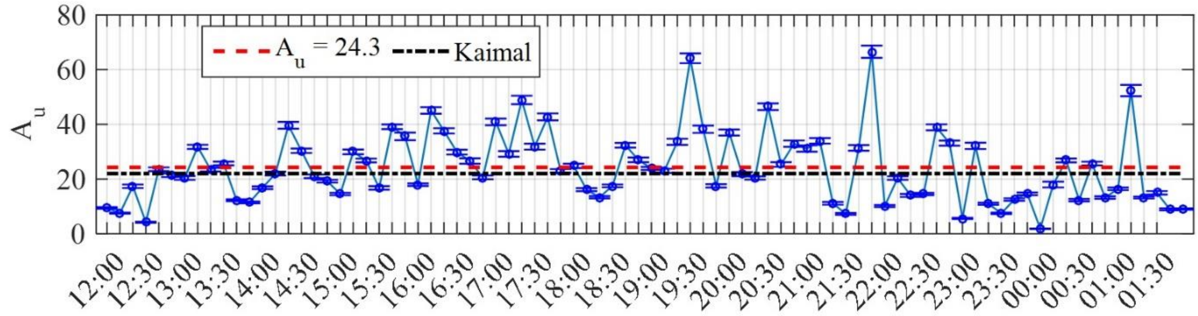

(b)

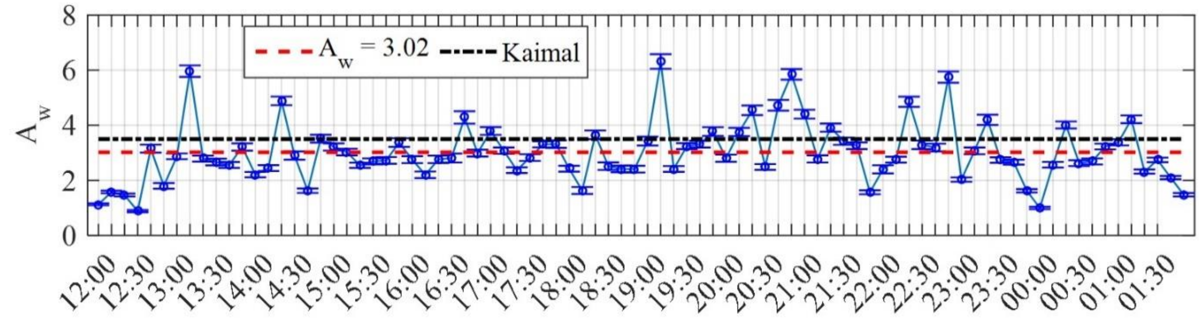

Fig. 20. Spectral parameters at the midspan: (a) A_u and (b) A_w (error bars show the 99% confidence intervals)

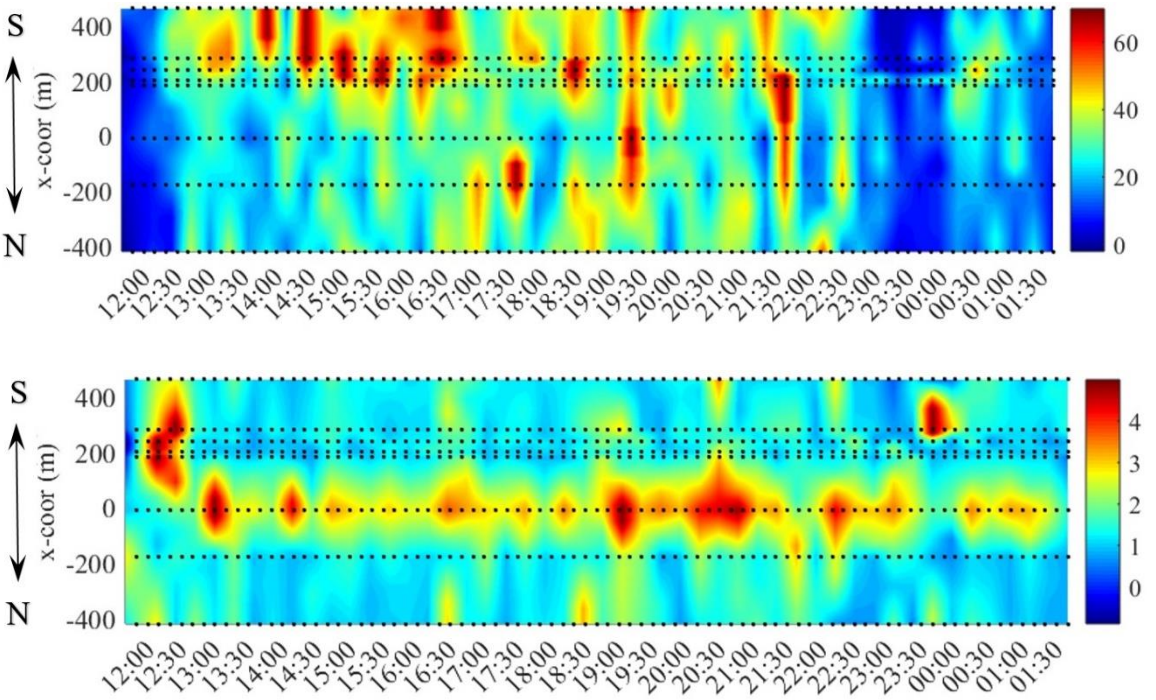

(a)

(b)

Fig. 21. Contour plots of spectral parameters: (a) A_u and (b) A_w

The parameters $A_{u,w}$ were then plotted against the previously obtained integral length scales for the recordings with mean speed higher than 15 m/s (Fig. 22). An apparent correlation is observed in the case of the along-wind component, where the measurements show random scatter for the vertical component.

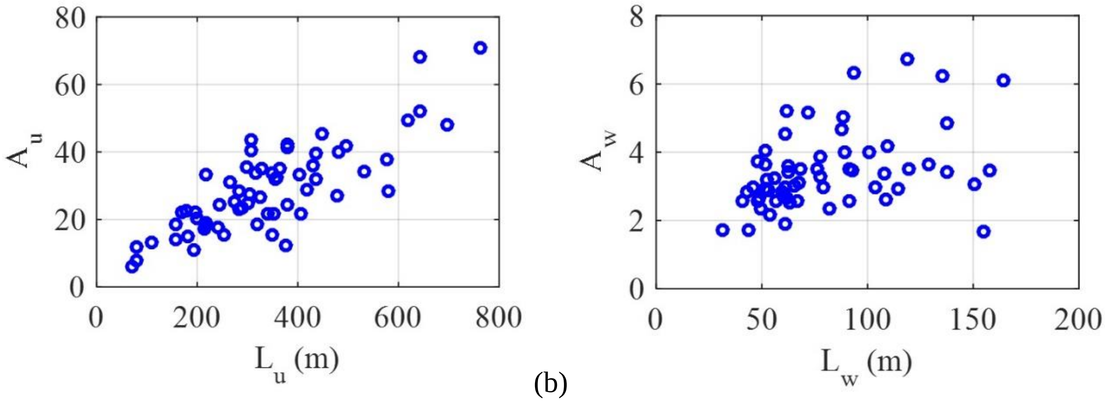

(a) (b)

Fig. 22. Spectral parameter vs. length scale: (a) along-wind turbulence and (b) vertical turbulence

4.9. Normalized cross-spectra of turbulence

In addition to the one-point statistics of turbulence, its spanwise correlation structure should be well defined for accurate prediction of the bridge dynamic response (Cheynet et al. 2016; Kristensen and Jensen 1979; Mann 2006; Toriumi et al. 2000). In the frequency domain, this is usually achieved with the help of a normalized cross-spectrum, which is essentially a frequency dependent cross-correlation coefficient. For two points along the bridge separated by a distance Δx, the normalized cross-spectral density is defined as

$$C_{mn}(f,\Delta x)=\frac{S_{mn}(f)}{\sqrt{S_m(f)S_n(f)}},\ \ n\in\{u,w\},\ \ m\in\{u,w\} \tag{4}$$

where S_{mn} is the cross-spectral density of turbulence at two points separated by Δx. Consequently, the normalized cross-spectral density can attain both negative and positive values and has real and imaginary parts. Its imaginary part includes the phase information and is usually neglected for separations normal to the wind direction (ESDU 2001; Simiu and Scanlan 1996).

Owing to the dense wind sensor network along the bridge span, the normalized cross-spectra of turbulence can be calculated for many separation distances. Using eight different sensor pair combinations, the normalized cross-spectra were calculated for the 10-minute recordings during the strong wind part of the storm (U > 15 m/s). The estimates for different sensor pairs are plotted against a non-dimensional frequency (f Δx / U) and shown in Fig. 23-Fig**. 25**. In the calculations, separation distances were taken as the distances between sensors, since wind direction was mostly perpendicular to the bridge longitudinal axis. Spectral estimations were carried out using Welch's method, as described in the previous section, which inevitably results in high variance in the estimates. Relying on the assumption that the process is ergodic, variance can be reduced by averaging estimates from different recordings. The average curves are also shown in the figures. The variance can also be reduced by fitting a parametric function to the scattered data. Visual inspection of the data suggests that a simple exponentially decaying function, such as the one used by Davenport (1961), would be appropriate. The expression is written as

$$C_{uu,ww}=\exp(-K_{u,w}\frac{f\Delta x}{U}) \tag{5}$$

where K is commonly referred to as the decay coefficient. The curves were fitted to the scatter data in the least-squares sense, and they are shown along with the data. The resulting decay coefficients are also indicated in the figures. Finally, only for the u-component, a theoretical expression by Krenk (1996) is also plotted on the measurement data for the sake of comparison. In case of the along-wind turbulence component, both the fitted exponential curves and the theoretical curve by Krenk show good agreement with the averaged normalized cross-spectra for small separations. However, as the distance between the sensors increases, deviations are apparent in the low reduced frequency range. Davenport's expression assumes full correlation at zero frequency, which is a known drawback of the simple function. Krenk's formula, on the other hand, gave lower correlation in the low frequency range compared to the averaged data. The discrepancy between the fitted exponential curves and measurement data is more profound in the case of vertical turbulence. The normalized cross-spectrum of u and w components were essentially zero, even for small separations.

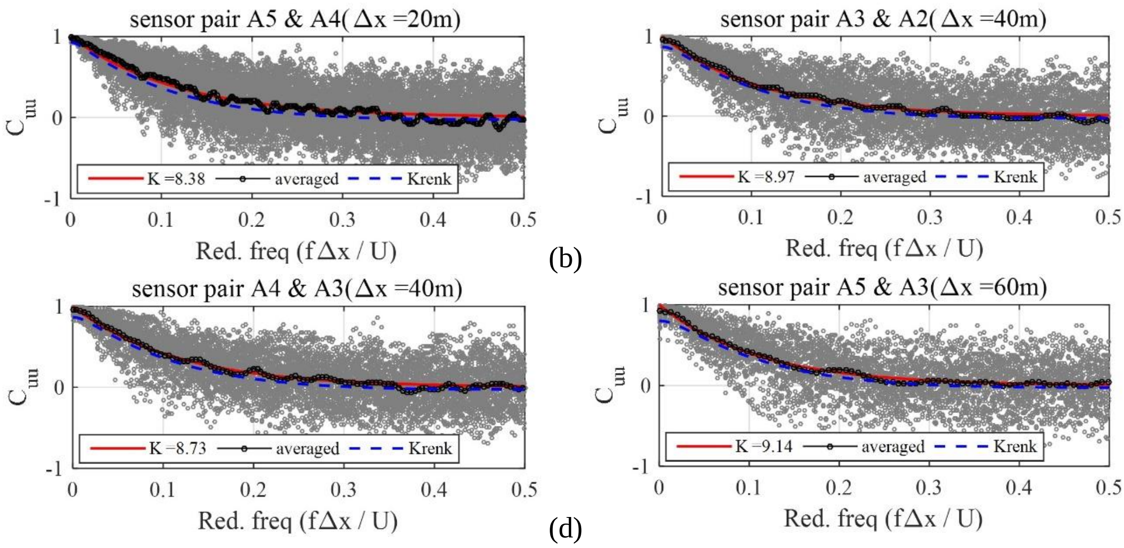

(a) (b)

(c) (d)

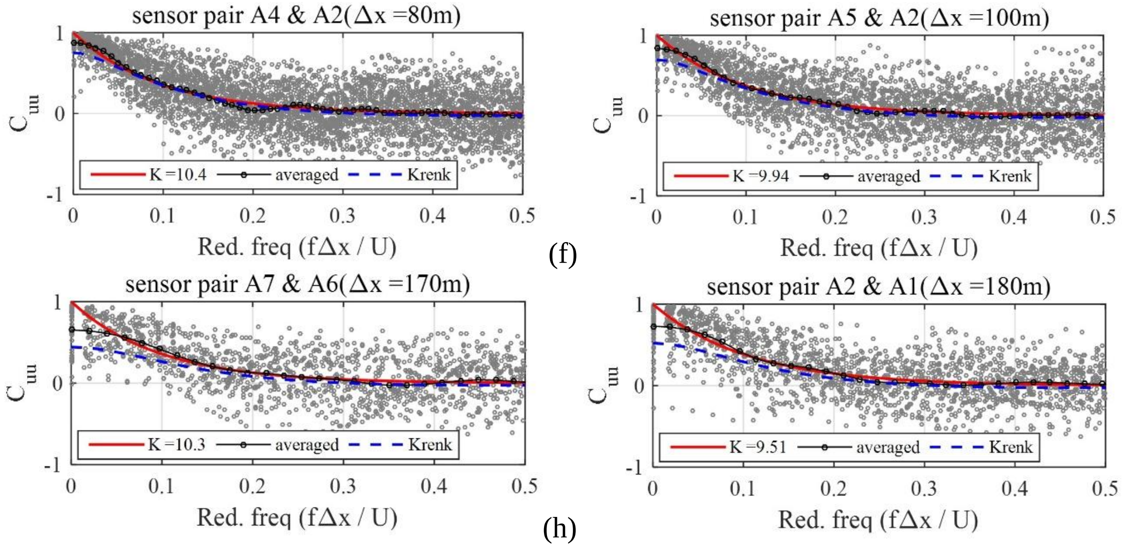

(e) (f)

(g) (h)

Fig. 23. Normalized cross-spectra of along-wind turbulence for several separation distances: (a) Δx = 20 m, (b) Δx = 40 m, (c) Δx = 40 m, (d) Δx = 60 m, (e) Δx = 80 m, (f) Δx = 100 m, (g) Δx = 170 m and (h) Δx = 180 m

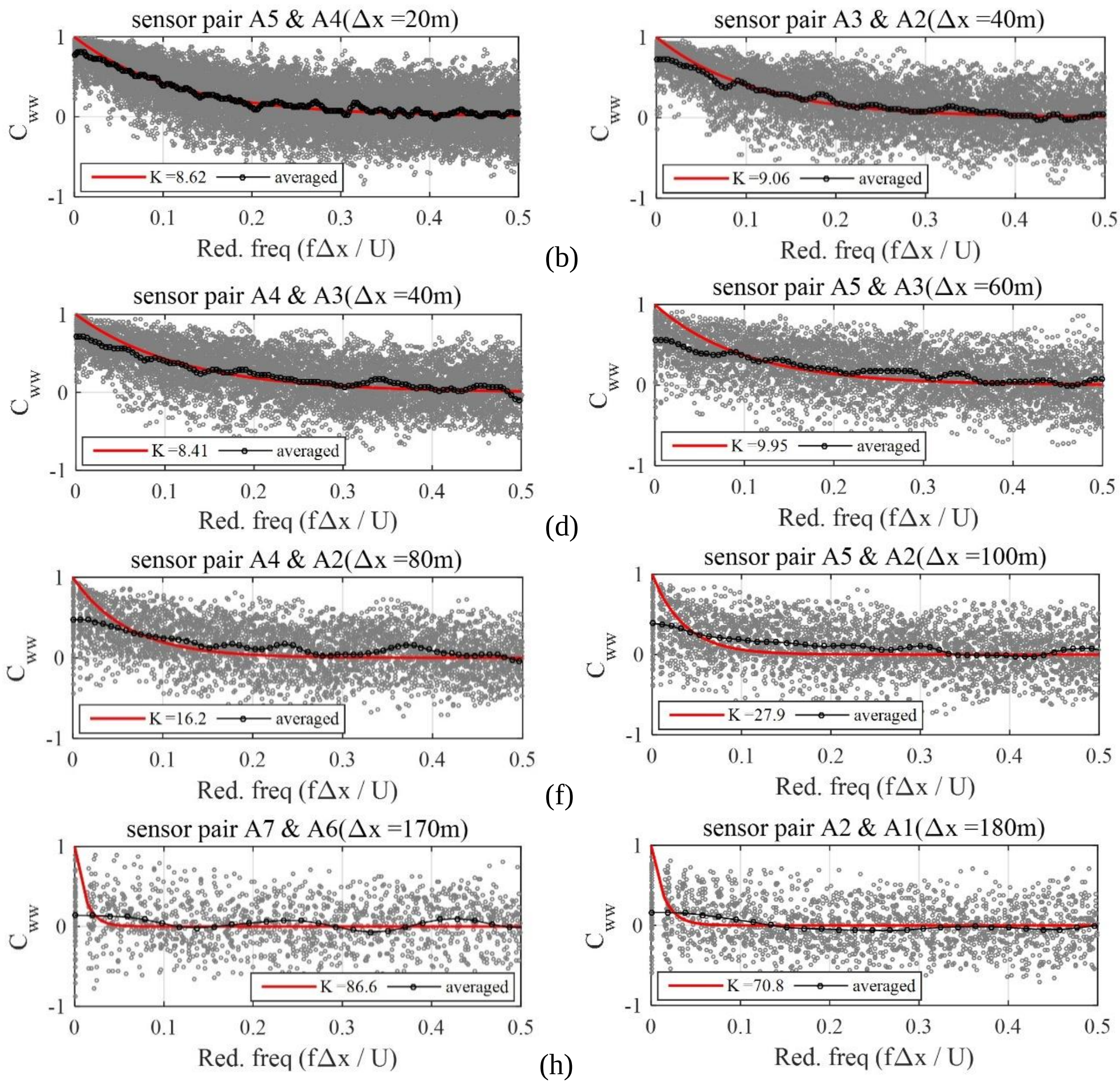

(a) (b)

(c) (d)

(e) (f)

(g) (h)

Fig. 24. Normalized cross-spectra of vertical turbulence for several separation distances: (a) Δx = 20 m, (b) Δx = 40 m, (c) Δx = 40 m, (d) Δx = 60 m, (e) Δx = 80 m, (f) Δx = 100 m, (g) Δx = 170 m and (h) Δx = 180 m

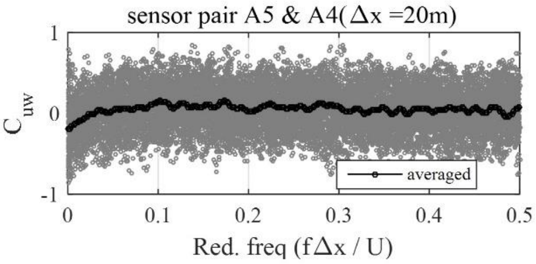

(a)

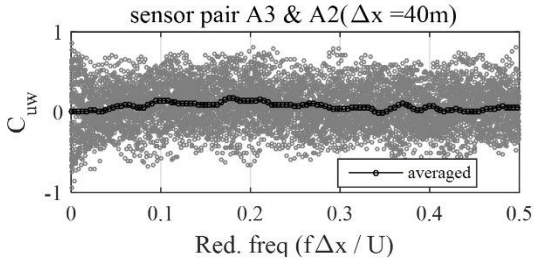

(b)

Fig. 25. Normalized cross-spectra of along-wind and vertical turbulence: (a) Δx = 20 m, (b) Δx = 40 m

Although the use of a dimensionless frequency in the x-axis is very useful here, it makes the interpretation of the results rather difficult since engineers are more interested in the corresponding frequencies. Therefore, the same data are also plotted in Fig. 26 in the form of contour plots by linearly interpolating the average normalized cross-spectra. The decrease in correlation with increasing frequency and distance is immediately observed. Fitted normalized cross-spectra with Davenport's formula are also given in the same form in Fig. 27. Here, it is easily observed that the discrepancy is restricted to the low-frequency range, i.e., frequencies lower than the lowest natural frequency of HB (0.05 Hz). Moreover, to overcome this drawback of Davenport's formula, a surface fit was made to the data given in Fig. 28 using the following two-parameter expression, which was also used in the design basis of the HB in the form of Krenk's formula:

$$C_{uu,ww}(f,\Delta x)=\left(1-\frac{1}{2}\kappa\Delta x\right)\exp(-\kappa\Delta x),\ \ \kappa=b_{u,w}\sqrt{\left(\frac{2\pi f}{U}\right)^2+\left(\frac{1}{c_{u,w}L_u}\right)^2} \tag{6}$$

where $b_{u,w}$ and $c_{u,w}$ are parameters to be fitted. The resulting contour plot is shown in Fig. 28. A very good agreement with the measurement data is achieved using Eqn. (6).

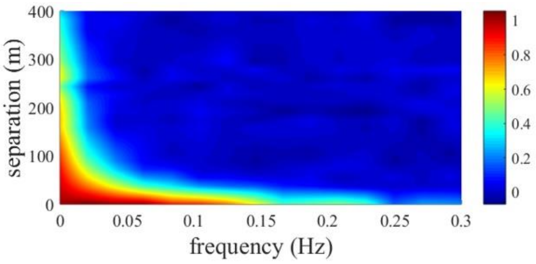

(a)

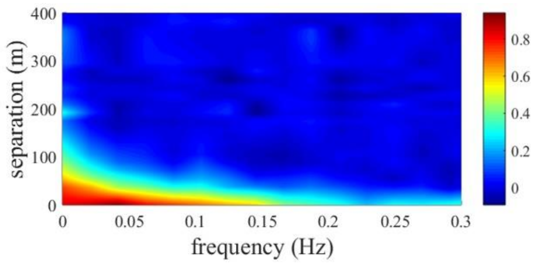

(b)

Fig. 26. Normalized cross-spectra of turbulence estimated from data (a) C_{uu} and (b) C_{ww}

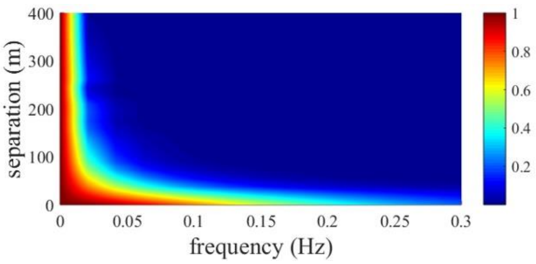

(a)

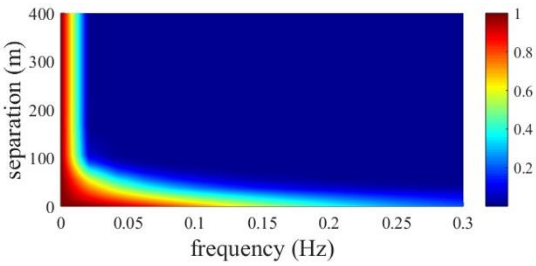

(b)

Fig. 27. Normalized cross-spectra of turbulence fitted to Davenport's formula in Eqn. (5): (a) C_{uu} and (b) C_{ww}

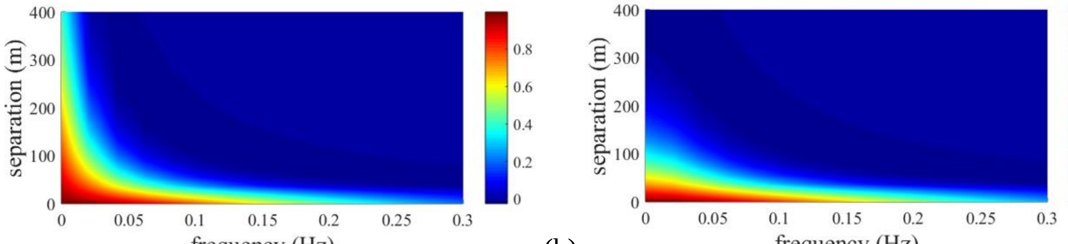

(a) (b)

Fig. 28. Normalized cross-spectra of turbulence fitted to Krenk-type formula in Eqn. (6): (a) C_{uu} and (b) C_{ww} ($b_u = 0.79$, $c_u = 1.44$, $b_w = 0.72$, $c_w = 0.27$)

Finally, the decay coefficients in Eqn. (5) were calculated for the 10-minute recordings separately using only the closely spaced sensor pairs. The results are presented in Fig. 29 with the 95% confidence intervals of the parameter estimates, where the mean value (for U > 15 m/s) and the N400 recommendation are also indicated. It is seen that the decay coefficients show random variation between 10-min recordings of the storm. The margin of uncertainity was higher for the larger decay coefficients (smaller correlation) for both components. In case of highly non-stationary recordings, the confidence intervals were usually larger.

(a)

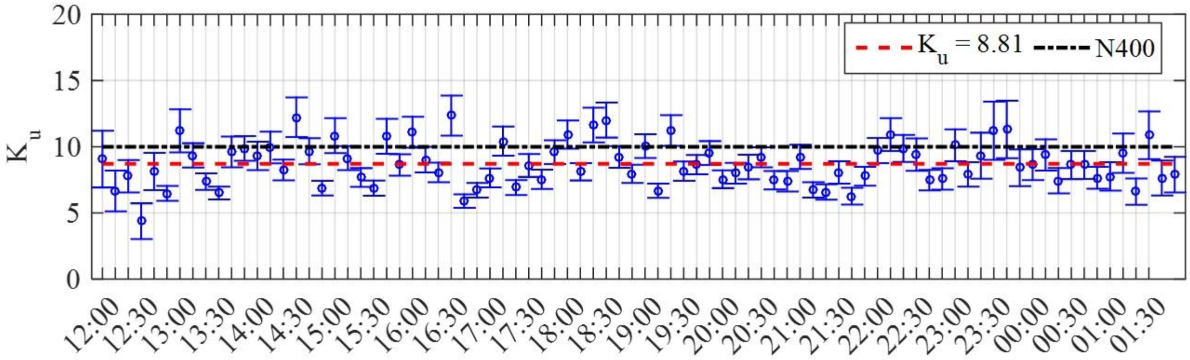

(b)

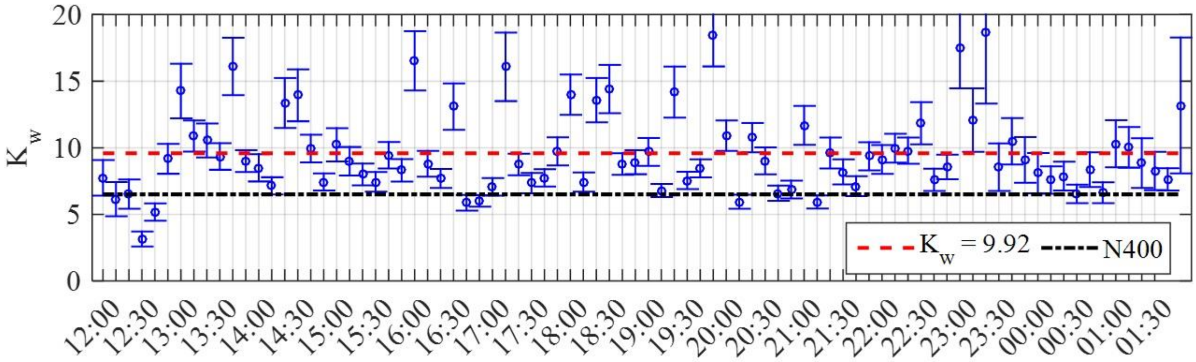

Fig. 29. Decay coefficients given in Eqn. (a) along-wind turbulence and (b) vertical turbulence

5. Buffeting response of the bridge deck

The dynamic response of the HB deck was measured using seven accelerometer pairs located along the bridge span (Table 1). The lateral and vertical accelerations were taken as the average of the signals from two sensors at either side of the girder, and torsional acceleration was obtained by dividing the difference of the two signals by the distance between them (13 meters). The acceleration signals were then low-pass filtered with a cut-off of 1 Hz to remove the high-frequency response, which is considered not important when the wind-induced vibrations are concerned. The continuous acceleration measurements from the sensor pair H3 (120 meters from the midspan) during the entire storm are given in Fig. 30. It is seen that in the beginning of the storm, when the mean wind speed was around 5 m/s, the acceleration response was very low. With the increase in wind speed around 12:30, the amplitude of vibrations rapidly increased. For all the response components, the highest sustained vibrations seem to have occurred between 17:00 – 19:30, where the wind was the strongest (Fig. 9). Two distinct, rather sudden peaks were also observed in all components, one around 14:50 and another around 16:50, which correspond to two strong gusts (Fig. 9). For a 10-minute recording, the probability distributions of accelerations are shown in Fig. 31. It is observed that all components follow a Gaussian distribution; therefore, the assumption of a zero-mean Gaussian response process seems fair.

(a)

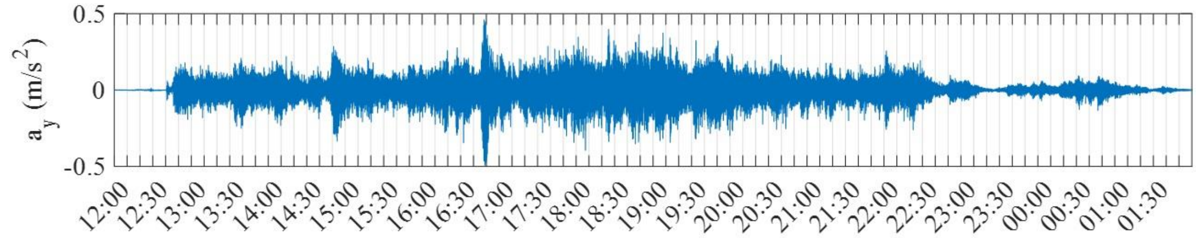

(b)

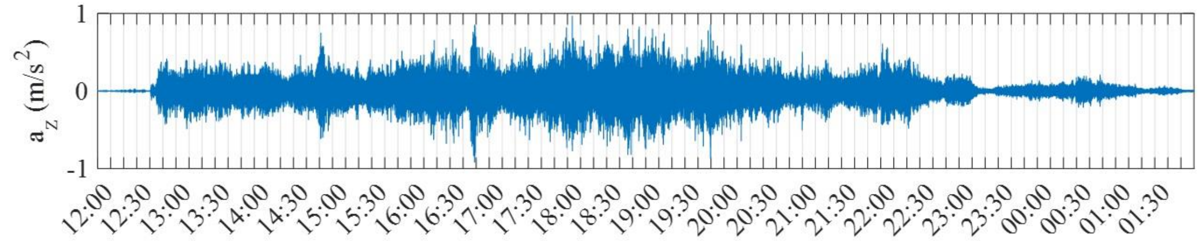

(c)

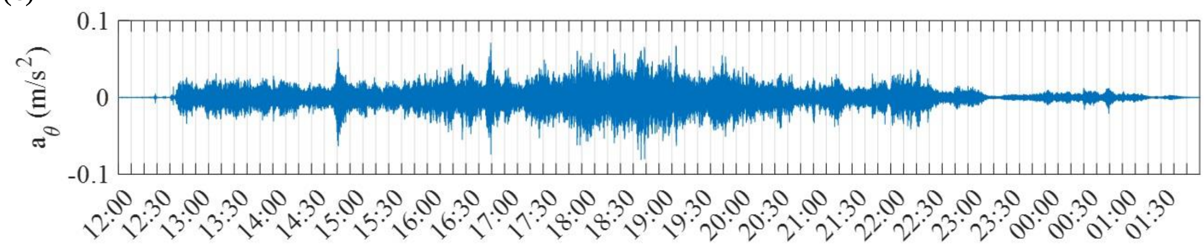

Fig. 30. Acceleration records at the quarter-span (using accelerometer pair H3) (a) lateral, (b) vertical and (c) torsional acceleration

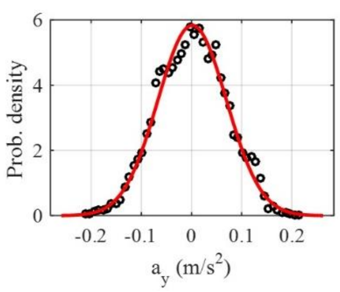

(a)

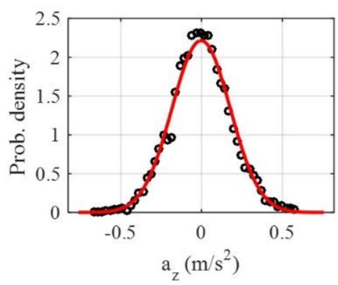

(b)

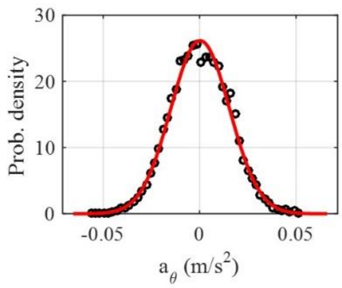

(c)

Fig. 31. Probability distributions of acceleration components at the midspan for a 10-minute recording recoded on 29/01/2016 between 18:40 and 18:50: (a) lateral, (b) vertical and (c) torsional components

In order to have a more elaborate look at the frequency content of the signals, short time Fourier transforms of the signals were carried out using 10-minute windows with 80% overlap between them, and the resulting spectrograms are presented in Fig. 32 for the three response components. Several frequency contributions, which were consistent throughout the storm, are apparent in the plots. The continuous horizontal lines in the plots for lateral (0.05 Hz, 0.1 Hz, 0.18 Hz), vertical (0.14 Hz, 0.21 Hz, 0.27 Hz, 0.33 Hz) and torsional (0.37 Hz, 0.42 Hz, 0.55 Hz) yield similar frequencies as the natural vibration frequencies of the bridge extracted through finite element analysis (Table 2). No significant change in vibration frequencies during the storm can be detected. The regions where the wind speed increases and decreases are distinguishable from the plots. Two vertical lines are also recognized, coinciding with the locations of the jumps in acceleration signals (Fig. 30).

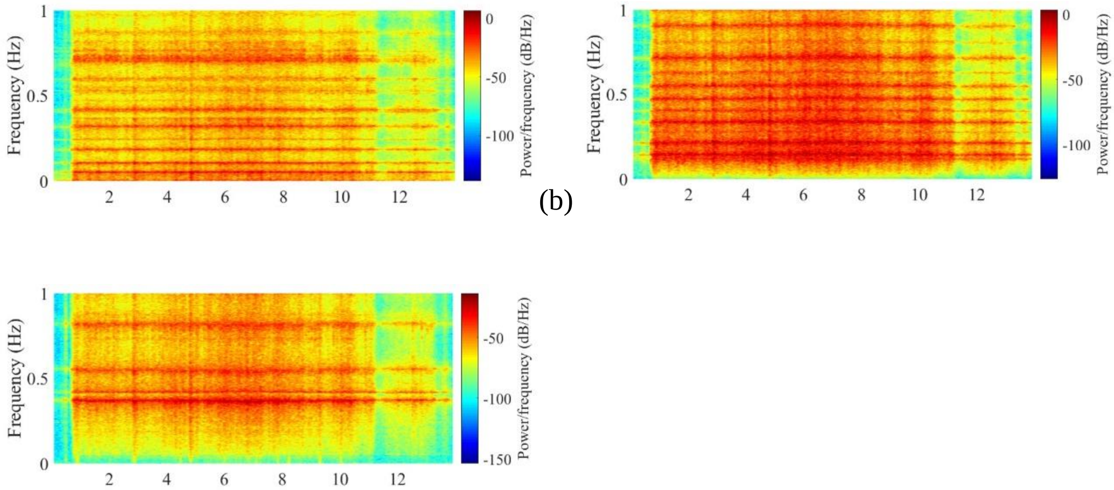

(a) (b) (c)

Fig. 32. Spectrogram of acceleration records at the quarter-span (using accelerometer pair H3): (a) lateral, (b) vertical and (c) torsional acceleration

Moreover, the root-mean-squares (RMSs) of the three response components were calculated for 10-minute recordings at each sensor pair location. The results are used to obtain contour plots of RMS acceleration and displacement responses, which are given in Fig. 33 and Fig. 34, respectively. Measurement locations are indicated on the plots as dots. According to the contour plots, the largest lateral response occurred around 16:30 – 16:50. Although this was not the interval with the highest wind speed, the wind was quite gusty, which can be seen from the plots of gust factor (Fig. 10) or turbulence intensity (Fig. 11). It can also be seen that higher modes are more important for the acceleration response, where displacement response is usually dominated by a few lower modes. For the lateral and torsional modes, first modes of vibration, which are symmetrical modes, dominated the responses, resulting in maximum displacements at the midspan. However, the vertical displacement response was maximum around the quarter-span rather than the midspan. This is because the first vertical mode is antisymmetric and more vibration modes contribute to the vertical response.

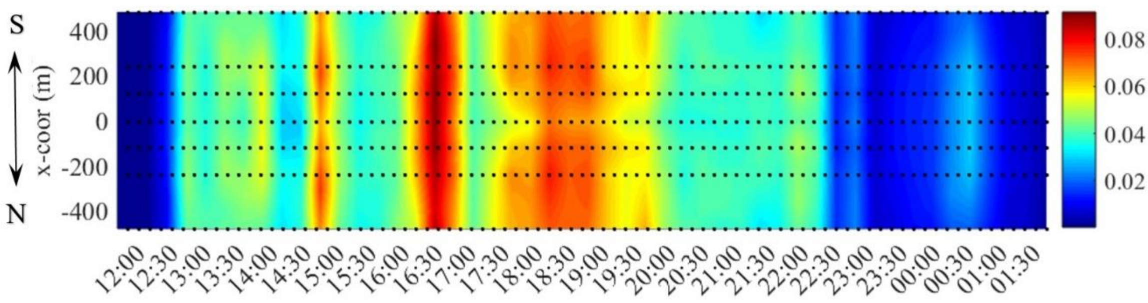

(a)

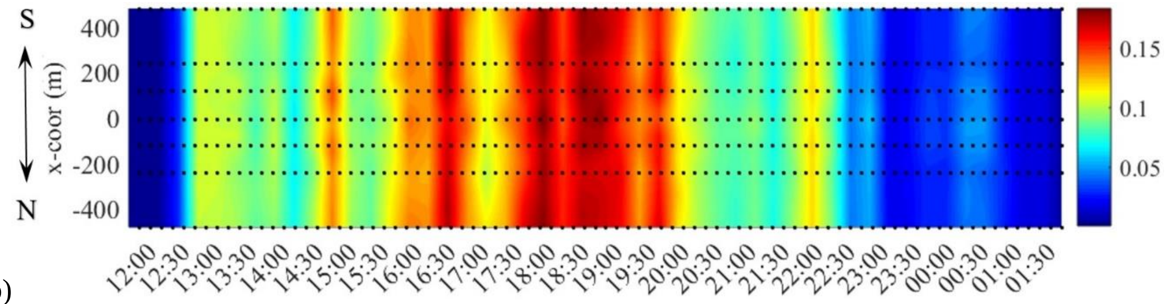

(b)

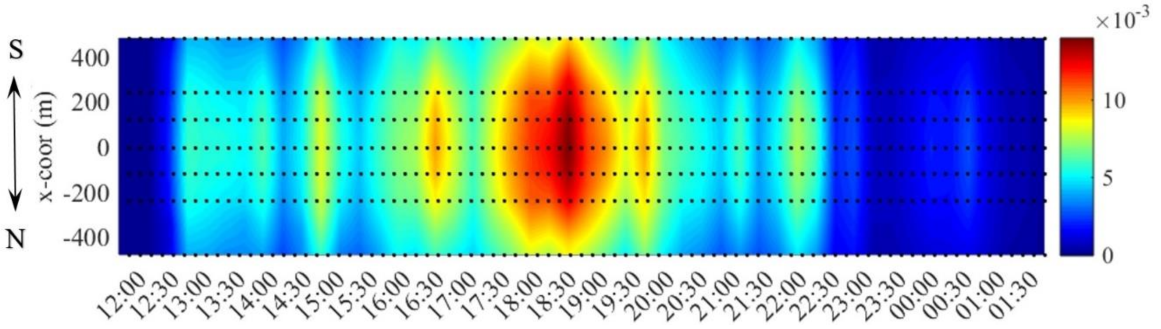

(c)

Fig. 33. RMS acceleration response during the storm (a) lateral (m/s^2), (b) vertical (m/s^2) and (c) torsional acceleration (rad/s^2)

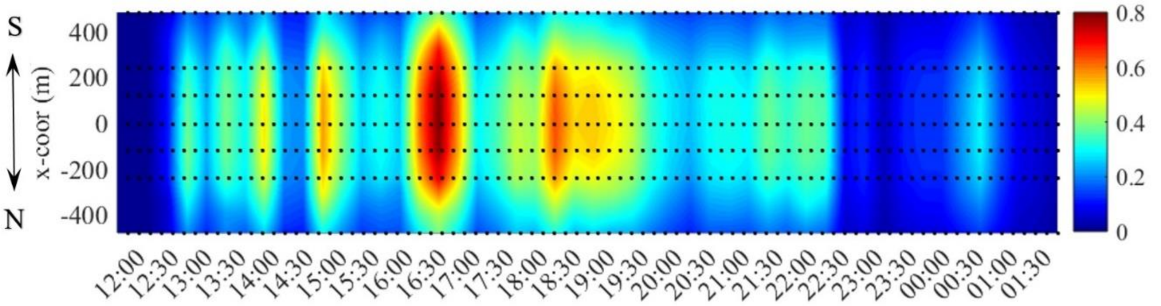

(a)

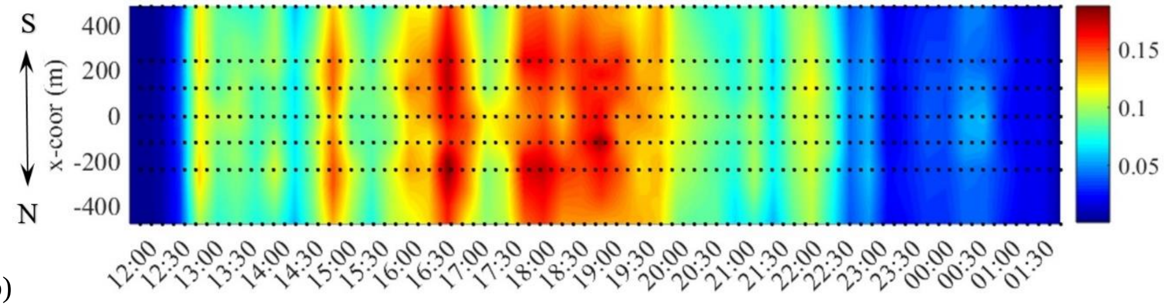

(b)

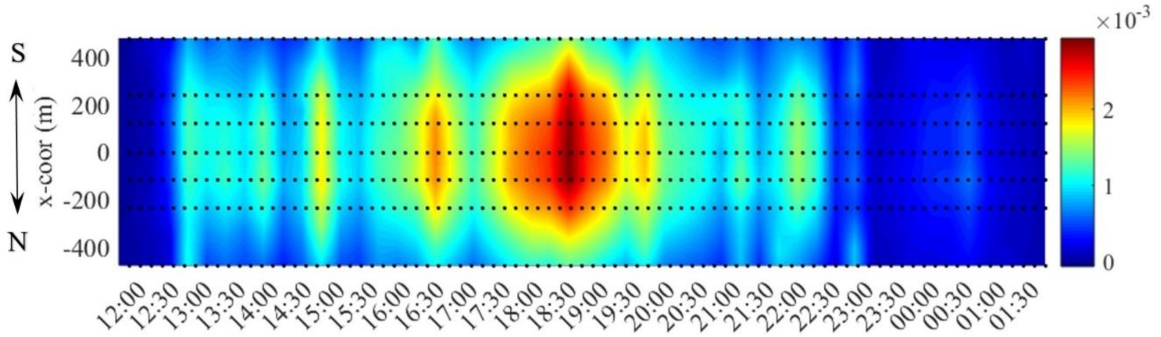

(c)

Fig. 34. RMS displacement response during the storm (a) lateral (m), (b) vertical (m) and (c) torsional displacement (rad)

It is also interesting to compare the results from this study on an extratropical cyclone to the results obtained from previous tropical cyclone measurements. Xu et al. (2001) studied the wind field characteristics and the dynamic response of the Tsing Ma Suspension Bridge in Hong Kong during the passage of typhoon Victor. The main span of the bridge is 1377 meters long, which is very similar to HB; however, the bridge girder is much wider (41 meters) and the bridge accommodates train passage. The topography surrounding the bridge is also complex, including sea, islands and mountains reaching up to 500 meters. From the wind measurements at the girder level, the typhoon was characterized with mean speeds up to 20 m/s and highly variable turbulence intensity. Along-wind length scales of 200-300 meters were reported, which are much lower than what was measured at the HB. Other differences include presence of skew-winds, high cross-wind turbulence, changing wind direction (due to passage of the eye of the typhoon) and variable angle-of-attack (-6° to +6°). The turbulence spectra could not be modeled well with von Karman or Kaimal spectra. The results suggest that it can be more challenging to model tropical storm winds. The maximum RMS accelerations of the bridge girder, on the other hand, were in general smaller than the case of HB under similar wind speeds, presumably due to its stiffer girder.

6. Comparison with analytical predictions

The buffeting response of the HB during Storm Tor was also evaluated analytically using a multimode approach. The fully coupled system of equations of motion including the aeroelastic terms were solved in the frequency domain using the procedure given in Øiseth et al. (2010), where the bridge displacements are written in terms of generalized coordinates of the still-air vibration modes. Detailed formulation of the procedure can be found elsewhere (Katsuchi et al. 1998; Øiseth et al. 2010) and, therefore, will not be repeated here. The first 80 still-air vibration modes of the bridge (0.05 Hz. – 1.3 Hz), which were obtained via finite element analysis, were included in the analysis, excluding the tower and cable modes. Petersen and Øiseth (2017) conducted sensitivity-based finite element model updating of the HB using monitoring data. It was seen that the discrepancy between identified and analytical natural frequencies were in an acceptable range for the applications in the current study. It should also be noted that the RMS response is more sensitive to damping, rather than minor shifts in the response frequencies. Information regarding the first few still-air modes is given in Table 2. A structural damping of 0.5% was assigned to all modes. The so-called self-excited forces, which are induced by the motion of the bridge deck, were modeled using aerodynamic derivatives (ADs). The ADs of the HB deck section were obtained by Siedziako et al. (2017) through forced vibration tests in the wind tunnel. The resulting ADs exhibited exceptionally low scatter, increasing confidence on the modeling of the self-excited forces. The ADs for the entire reduced velocity range were obtained by fitting rational functions to the experimental data by nonlinear least squares approximation. The identified ADs and the corresponding fits were presented in Figs.17 and 18 in Fenerci and Øiseth (2017). The steady-state force coefficients were also obtained using the tests by Siedziako et al. (2017) in the wind tunnel (Table 3). The cross-sectional aerodynamic admittance functions were set to unity due to lack of experimental data, and the spanwise correlation of the buffeting forces was assumed the same as those of the incoming turbulence.

Table 2
Mode shapes and natural frequencies from FEM

Lateral			Vertical			Torsional		
mode no	freq. (Hz)	description	mode no	freq. (Hz)	description	mode no	freq. (Hz)	description
1	0.05	1st symm.	3	0.11	1st asymm.	15	0.36	1st symm.
2	0.098	1st asymm.	4	0.14	1st symm.	26	0.52	1st asymm.
5	0.169	2nd symm.	6	0.197	2nd symm.			
10	0.233	2nd asymm.	7	0.21	2nd asymm.			
11	0.244	3rd symm.	12	0.272	3rd symm.			
13	0.293	3rd asymm.	14	0.33	3rd asymm.			

Table 3

Steady-state force coefficients for the Hardanger Bridge section (Siedziako et al. 2017)

$\bar{C}_D$	C'_D	$\bar{C}_L$	C'_L	$\bar{C}_M$	C'_M
1.05	0	-0.363	2.22	-0.017	0.786

* D = drag, L = lift, M = moment (bar denotes mean value and apostrophe denotes derivative)

Neglecting the cross terms, the cross-spectral density matrix of turbulence used in the analysis can be written as

$$S_{turb}(\Delta x, f) = \begin{bmatrix} S_{uu}(\Delta x, f) & 0 \\ 0 & S_{ww}(\Delta x, f) \end{bmatrix}, \quad S_{uu,ww}(\Delta x, f) = S_{u,w}(f) C_{uu,ww}(f, \Delta x) \tag{7}$$

where $S_{u,w}(f)$ are given in Eqn. (3) and $C_{uu,ww}(f, \Delta x)$ in Eqn. (5). The values of the spectral parameter $A_{u,w}$ and the decay coefficient $K_{u,w}$ in the equations were taken from Fig. 20 and Fig. 29, respectively, for each 10-minute recording. It should be noted that this formulation assumes spanwise uniform turbulence characteristics, which is not the case for the HB. The spanwise non-uniformity of the mean wind speed, turbulence intensities and spectral parameters can be implemented by modifying the cross-spectral density matrix in Eqn. (7) as follows:

$$\begin{gathered} \tilde{S}_{turb}(x_1, x_2, f) = \begin{bmatrix} S_{uu}(x_1, x_2, f) & 0 \\ 0 & S_{ww}(x_1, x_2, f) \end{bmatrix}, \\ S_{uu,ww}(x_1, x_2, f) = \sqrt{S_{u,w}(x_1, f) S_{u,w}(x_2, f)}\, C_{uu,ww}(f, \Delta x) \end{gathered} \tag{8}$$

where $S_{u,w}(x_1, f)$ and $S_{u,w}(x_2, f)$ are the auto-spectral densities of turbulence components at two points x_1 and x_2, separated by Δx. The buffeting response of the HB was calculated using both spanwise uniform and non-uniform wind profiles. In the non-uniform case, the mean wind speed, turbulence intensities and spectral parameters $A_{u,w}$ were interpolated between sensor locations to obtain the profiles, where the normalized cross-spectra of turbulence was kept constant.

The comparisons of measured and predicted responses are given in Fig. 35 and Fig. 36 for the RMS acceleration response and Fig. 37 and Fig. 38 for the RMS displacement response at the midspan. It should be noted that for a fair comparison between RMS responses, the analytical response spectra was integrated up to a frequency of 1 Hz. The comparisons yield similar results for the RMS acceleration and displacement responses; therefore, a common discussion is possible. The lateral and torsional RMS responses were predicted with reasonable accuracy, although the variability in the lateral response was not fully captured with the analytical method. This can be attributed to the lack of wind forces on bridge cables and towers in the analysis. This issue was also addressed in Fenerci and Øiseth (2017). The vertical response, on the other hand, was severely underestimated by the analysis for the whole storm. The source of this discrepancy cannot be easily identified since many sources of uncertainty are present in the analysis. However, the analysis seems to capture the variability in response reasonably well (Fig. 36 and Fig. 38). Considering this and given that the turbulence field was modeled with maximum possible accuracy, it is unlikely that the discrepancy is due to uncertainties in the wind field model. The difference between uniform and non-uniform analyses were negligible, especially compared to the overall uncertainty involved in the predictions.

The total modal damping ratios utilized in the analysis are presented in Fig. 39. Petersen and Øiseth (2017) developed an operational modal analysis (OMA) framework to identify the natural frequencies of HB based on covariance-driven stochastic subspace identification (SSI) method (Peeters and De Roeck 2001). Applying the same framework here, total modal damping ratios during two one-hour segments of the storm were identified. The comparison of identified damping ratios and damping ratios utilized in the analysis are given in Table 4. To distinguish between structural and aerodynamic damping, SSI was performed on a low wind speed (≈3 m/s) recording (recorded on 20/12/2015 01.30-2.30) and identified damping ratios were assumed as structural damping. Looking at the comparison, it is seen that the horizontal and torsional damping were modeled with reasonable accuracy, where the damping in vertical modes were underestimated in the analysis. This implies even higher discrepancy between measured and calculated vertical response, which is contradictory and indicates further problems in prediction of the vertical response.

Table 4
Identified vs. analytical modal damping ratios

	16.00-17.00						18.00-19.00					
	ζ_{str} (%)		ζ_{aero} (%)		ζ_{tot} (%)		ζ_{str} (%)		ζ_{aero} (%)		ζ_{tot} (%)	
Mode	ANA	SSI	ANA	SSI	ANA	SSI	ANA	SSI	ANA	SSI	ANA	SSI
H1	0.50	0.88	1.01	0.27	1.51	1.15	0.50	0.88	1.25	0.53	1.75	1.41
H2	0.50	0.79	0.64	0.37	1.14	1.16	0.50	0.79	0.75	0.49	1.25	1.28
V1	0.50	1.70	3.59	3.48	4.09	5.18	0.50	1.70	4.67	5.07	5.17	6.77
V2	0.50	0.16	2.57	4.19	3.07	4.35	0.50	0.16	3.42	6.24	3.92	6.40
H3	0.50	0.47	0.39	0.08	0.89	0.55	0.50	0.47	0.46	0.68	0.96	1.15
V3	0.50	0.14	1.51	3.00	2.01	3.14	0.50	0.14	2.05	3.80	2.55	3.94
V4	0.50	0.33	1.34	1.99	1.84	2.32	0.50	0.33	1.82	3.03	2.32	3.36
V5	0.50	0.19	0.90	1.67	1.40	1.86	0.50	0.19	1.21	1.96	1.71	2.15
H4	0.50	0.22	0.24	0.38	0.74	0.60	0.50	0.22	0.28	0.53	0.78	0.75
V6	0.50	0.22	0.67	1.28	1.17	1.50	0.50	0.22	0.90	1.38	1.40	1.60
T1	0.50	0.25	0.08	0.85	0.58	1.10	0.50	0.25	0.11	0.58	0.61	0.83
T2	0.50	0.76	0.05	0.74	0.55	1.50	0.50	0.76	0.06	0.89	0.56	1.65

*H: Horizontal mode, V: vertical mode, T: torsional mode, ζ_{str} : structural modal damping ratio, ζ_{aero} : aerodynamic modal damping ratio, ζ_{tot} : total modal damping ratio, ANA: analysis, SSI: stochastic subspace identification

When the analyses were repeated to take into account the angle-of-attack shown in Fig. 16 using steady-state force coefficients for an inclined section of 3° (Table 5), no significant change was observed in the lateral and torsional responses. The vertical response, however, was found to be even smaller, resulting into an even larger discrepancy when compared with the measurements. Unfortunately, the section of Siedziako et al. (2017) were not tested to obtain ADs for an angle-of-attack. However, ADs corresponding to a 3° angle-of-attack was obtained through free vibration tests of Hansen et al. (2006) on the HB section in a different wind tunnel prior to the design of the bridge. The analyses were repeated using the ADs of Hansen et al. (2006) for the cases of 0° and 3° angle-of-attack. Again, the change in the predicted responses between the two cases were not significant.

Table 5
Steady-state force coefficients for the Hardanger Bridge section for an angle-of-attack of 3° (Siedziako et al. 2017)

$\bar{C}_D$	C'_D	$\bar{C}_L$	C'_L	$\bar{C}_M$	C'_M
1.082	0.94	-0.267	1.302	0.021	0.698

* D = drag, L = lift, M = moment (bar denotes mean value and apostrophe denotes derivative)

(a)

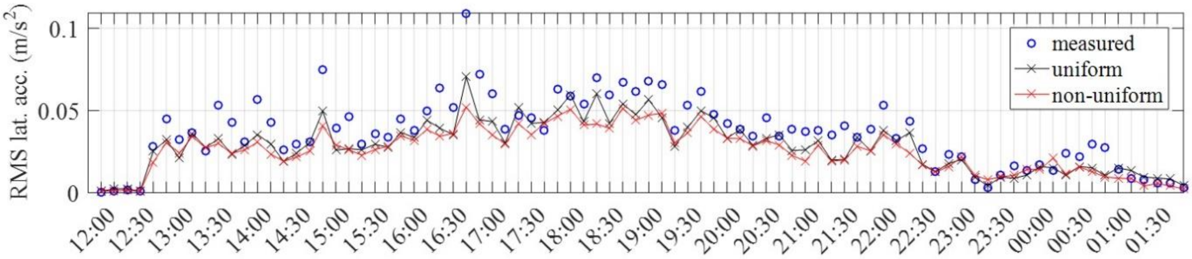

(b)

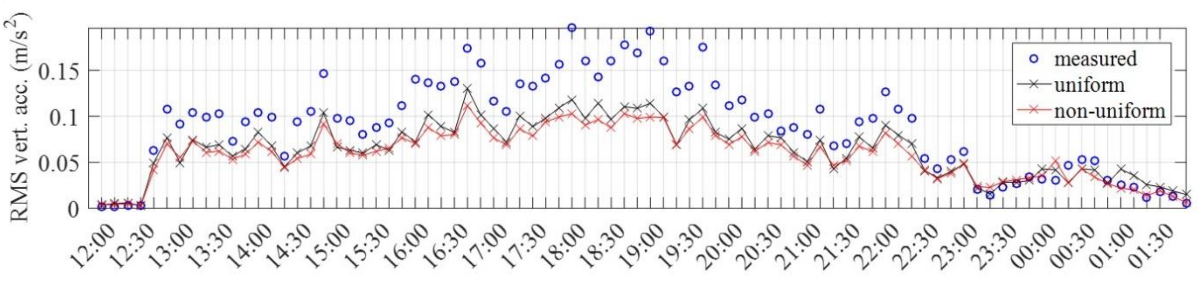

(c)

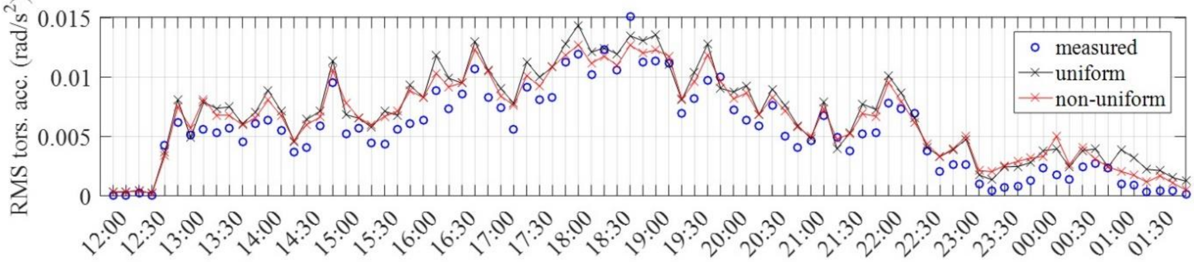

Fig. 35. RMS acceleration response comparison (a) lateral, (b) vertical and (c) torsional acceleration

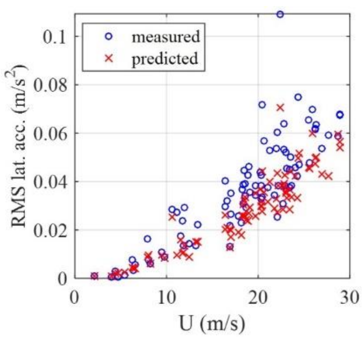

(a)

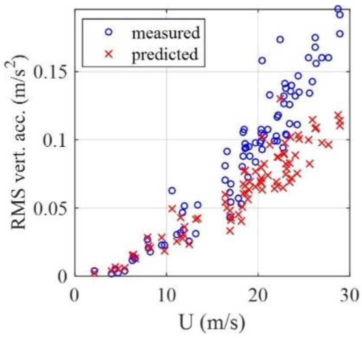

(b)

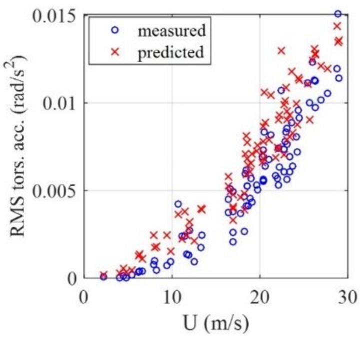

(c)

Fig. 36. RMS acceleration vs. mean wind speed comparison (a) lateral, (b) vertical and (c) torsional acceleration

(a)

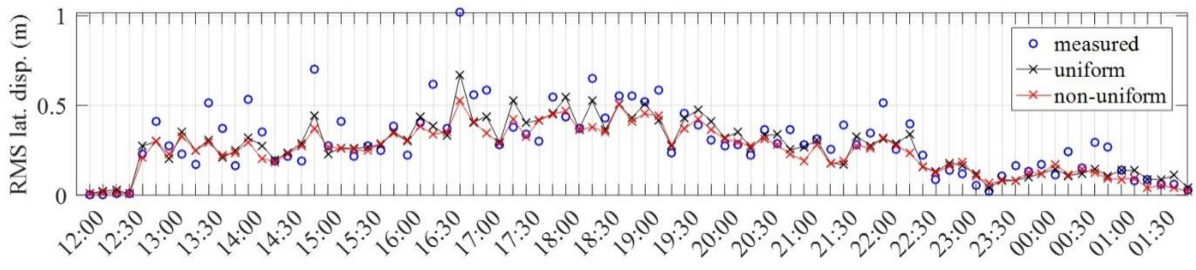

(b)

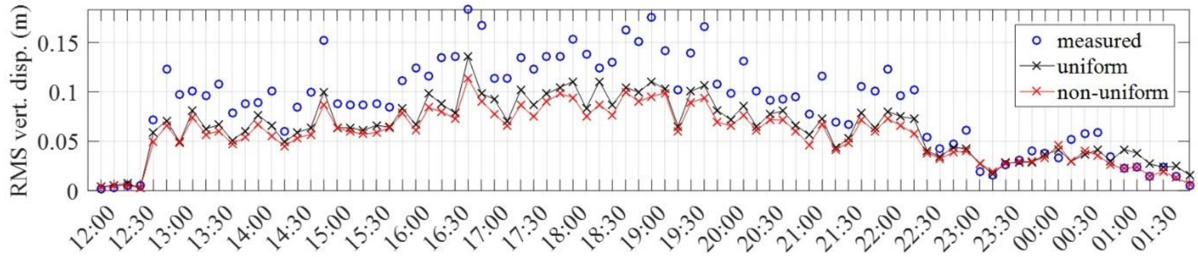

(c)

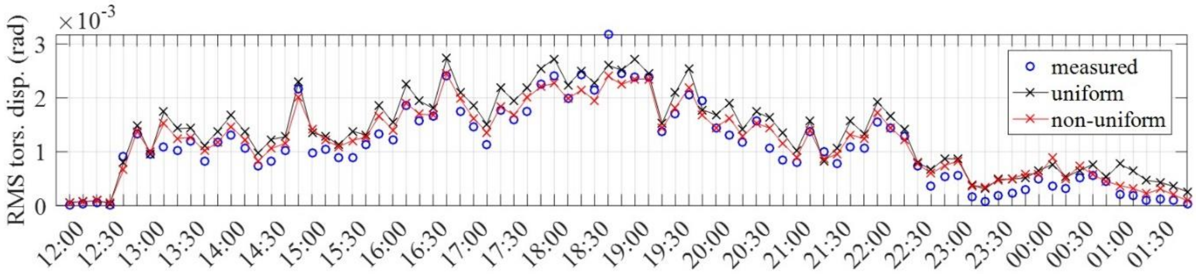

Fig. 37. RMS displacement response comparison (a) lateral, (b) vertical and (c) torsional displacement

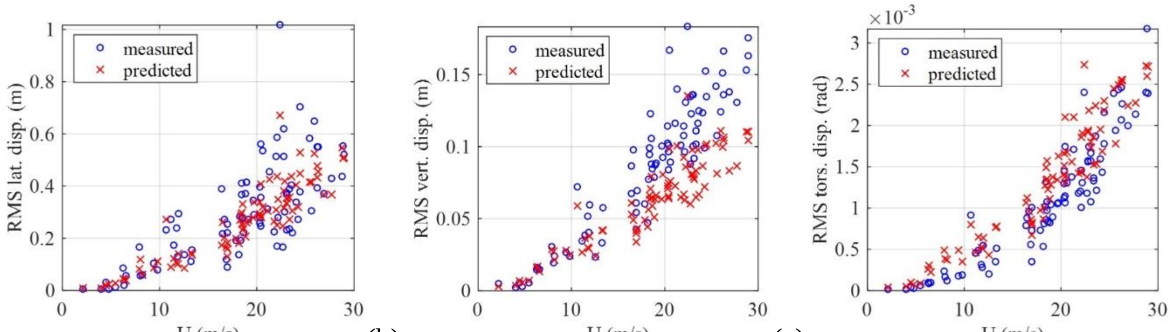

(a) (b) (c)

Fig. 38. RMS displacement vs. mean wind speed comparison (a) lateral, (b) vertical and (c) torsional displacement

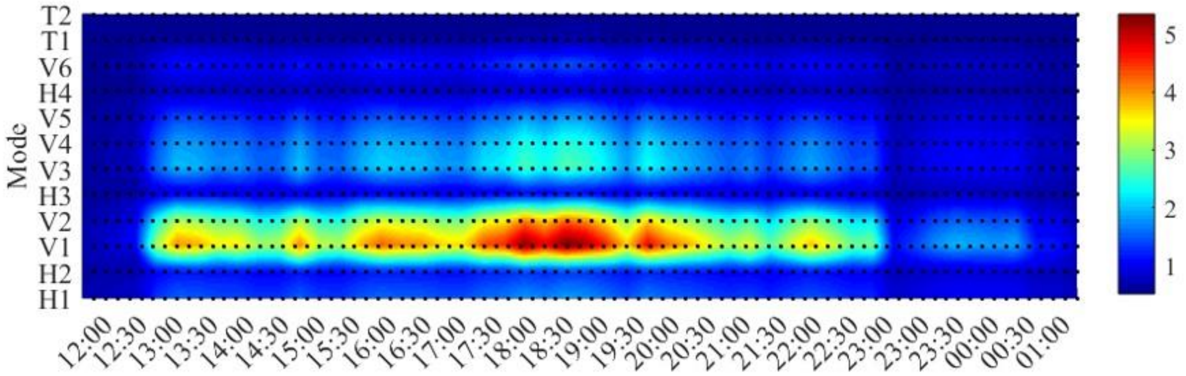

Fig. 39. Modal total damping ratio utilized in the analysis (%)

Although the RMS response at the midspan is a good indicator of the accuracy of the predictions from a global point of view, it is also of interest to see how the spectral densities and responses at different locations along the bridge correspond between measurement data and analytical results. Therefore, a 10-minute recording with high wind speed and response was selected, and its acceleration response spectra at the span and spanwise RMS acceleration response were compared to the analytical predictions in Fig. 40 and Fig. 41, respectively. It is seen that the discrepancy in the vertical RMS response mainly arises from the underestimation of both magnitude and bandwidth of the first mode spectral response. It is also observed that even though the RMS responses of lateral and torsional responses were predicted with reasonable accuracy, significant discrepancies were present in the high frequency range of the two spectra. Furthermore, the peaks of the response spectra were also not matched well by the analysis, especially beyond 0.5 Hz. Thus, the prediction of higher frequency response (>0.5 Hz) appears to be more challenging in the absence of aerodynamic admittance information and a more accurate description of the modal properties corresponding to such modes.

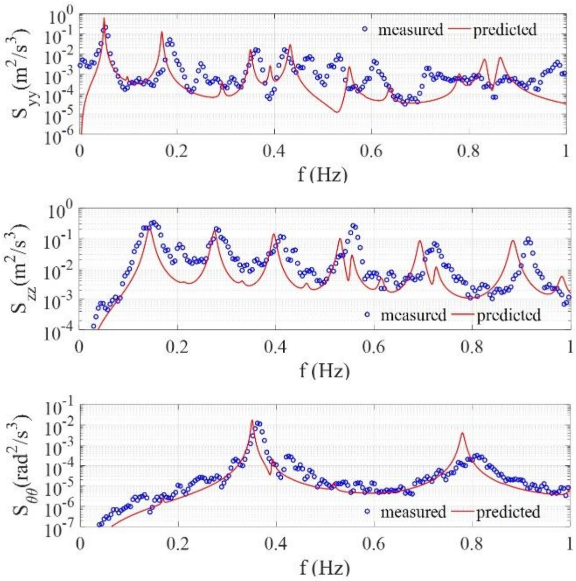

(a)

(b)

(c)

Fig. 40. Comparison of spectral density of the acceleration response at the midspan for a 10-minute recording recoded on 29/01/2016 between 18:40 and 18:50: (a) lateral, (b) vertical and (c) torsional acceleration.

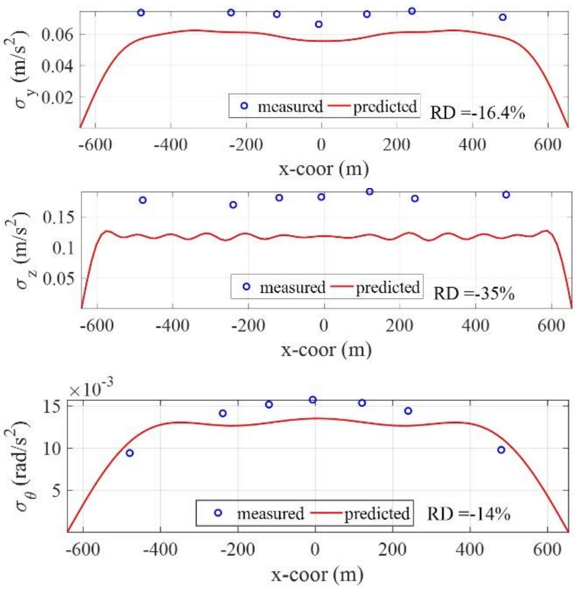

(a)

(b)

(c)

Fig. 41. Comparison of RMS acceleration response along the bridge span for a 10-minute recording recoded on 29/01/2016 between 18:40 and 18:50: (a) lateral, (b) vertical and (c) torsional acceleration. (RD = relative discrepancy)

7. Conclusions

Strong wind characteristics and dynamic response of a long-span suspension bridge located in mountainous terrain were studied in this paper using full-scale monitoring data acquired during a storm. The dynamic response of the bridge deck was predicted analytically and compared with the measured response. The following conclusions were reached for this specific case:

- The wind recordings showed non-stationary features, especially in the beginning and the end of the strong wind part of the storm. The along-wind and vertical turbulence components exhibited a nearly Gaussian distribution, where the cross-wind turbulence did not.
- Length scale estimations using Taylor's hypothesis showed significant variability and did not agree with the code recommendations. The use of length scales as deterministic design parameters should be avoided when possible, especially in complex terrain and non-stationary wind.
- It was shown that the one-point spectra of the turbulence could be represented reasonably well by a Kaimal-type of spectral formula. Despite its well-known weaknesses, Davenport's formula was found satisfactory in representing the normalized cross-spectra of turbulence in the important reduced frequency range.
- Comparisons between measured and predicted responses yielded significant discrepancies in case of the vertical response component. Reasonable agreement was achieved in case of lateral and torsional response predictions. Moreover, it was found more challenging to match the spectral response compared to the RMS response.
- The use of spanwise non-uniform profiles for the turbulence statistics did not improve the results significantly, considering the overall uncertainty in the predictions.

8. Acknowledgments

The research described in this paper was financially supported by the Norwegian Public Roads Administration. The authors also thank PhD candidate Øyvind Wiig Petersen for his valuable help in damping identification.

9. References

Bendat, J., and Piersol, A. (2000). "Random Data Analysis and Measurement Procedures." *Measurement Science and Technology*.

Bietry, J., Delaunay, D., and Conti, E. (1995). "Comparison of full-scale measurement and computation of wind effects on a cable-stayed bridge." *Journal of Wind Engineering and Industrial Aerodynamics*, 57(2–3), 225–235.

Brownjohn, J. M. W., Bocciolone, M., Curami, A., Falco, M., and Zasso, A. (1994). "Humber bridge full-scale measurement campaigns 1990-1991." *Journal of Wind Engineering and Industrial Aerodynamics*, 52(C), 185–218.

Cao, S., Tamura, Y., Kikuchi, N., Saito, M., Nakayama, I., and Matsuzaki, Y. (2009). "Wind characteristics of a strong typhoon." *Journal of Wind Engineering and Industrial Aerodynamics*, 97(1), 11–21.

Cao, S., Tamura, Y., Kikuchi, N., Saito, M., Nakayama, I., and Matsuzaki, Y. (2015). "A case study of gust factor of a strong typhoon." *Journal of Wind Engineering and Industrial Aerodynamics*, 138, 52–60.

Chen, J., Hui, M. C. H., and Xu, Y. L. (2007). "A comparative study of stationary and non-stationary wind models using field measurements." *Boundary-Layer Meteorology*, 122(1), 105–121.

Chen, X. (2015). "Analysis of multimode coupled buffeting response of long-span bridges to nonstationary winds with force parameters from stationary wind." *Journal of Structural Engineering (United States)*, 141(4), 1–14.

Chen, X., Kareem, A., and Matsumoto, M. (2001). "Multimode coupled flutter and buffeting analysis of long span bridges." *Journal of Wind Engineering and Industrial Aerodynamics*, 89(7–8), 649–664.

Cheynet, E., Jakobsen, J. B., and Snæbjørnsson, J. (2016). "Buffeting response of a suspension bridge in complex terrain." *Engineering Structures*, 128, 474–487.

Choi, E. C. C. (1978). "Characteristics of typhoons over the South China Sea." *Journal of Wind Engineering and Industrial Aerodynamics*, 3(4), 353–365.

Choi, E. C. C. (1983). *Wind Loading in Hong Kong—Commentary on the Code of Practice on Wind Effects Hong Kong*. Hong Kong Institute of Engineers, Hong Kong.

Cross, E. J., Koo, K. Y., Brownjohn, J. M. W., and Worden, K. (2013). "Long-term monitoring and data analysis of the Tamar Bridge." *Mechanical Systems and Signal Processing*, 35(1–2), 16–34.

Davenport, A. G. (1961). "The spectrum of horizontal gustiness near the ground in high winds." *Quarterly Journal of the Royal Meteorological Society*, 87(372), 194–211.

Davenport, A. G. (1962). "Buffeting of a suspension bridge by storm winds." *Journal of structural Division*, 88(3), 233–268.

Ellevset, O., and Skorpa, L. (2011). *A feasibility study – How to cross the wide and deep Sognefjord, summary*. Norwegian Public Roads Administration - Western Region Projects Division, Norway.

ESDU 086010. (2001). *Characteristics of atmospheric turbulence near the ground Part 3: variations in space and time for strong winds (neutral atmosphere)*. ESDU International plc, London.

ESDU 85020. (2001). *Characteristics of atmospheric turbulence near groud Part 2: signle point data for strong winds (neutral atmosphere)*. ESDU International plc, London.

Fenerci, A., and Øiseth, O. (2016a). "Wind Field Characteristics at the Hardanger Bridge Site." *Proceedings of the 12th UK Conference on Wind Engineering*, Nottingham, UK.

Fenerci, A., and Øiseth, O. (2016b). "Full-Scale Measurements on the Hardanger Bridge During Strong Winds." *Dynamics of Civil Structures, Volume 2: Proceedings of the 34th IMAC, A Conference and Exposition on Structural Dynamics 2016*, S. Pakzad and C. Juan, eds., Springer International Publishing, Cham, 237–245.

Fenerci, A., and Øiseth, O. (2017). "Measured Buffeting Response of a Long-Span Suspension Bridge Compared with Numerical Predictions Based on Design Wind Spectra." *Journal of Structural Engineering (United States)*, 143(9).

Fenerci, A., Øiseth, O., and Rønnquist, A. (2017). "Long-term monitoring of wind field characteristics and dynamic response of a long-span suspension bridge in complex terrain." *Engineering Structures*, 147, 269–284.

Hansen, S., Lollesgaard, M., Rex, S., Jacobsen, J., and Hansen, E. (2006). *The Hardanger Bridge: Static and Dynamic Wind Tunnel Tests with A Section Model*. Copenhagen.

Harstveit, K. (1996). "Full scale measurements of gust factors and turbulence intensity, and their relations in hilly terrain." *Journal of Wind Engineering and Industrial Aerodynamics*, 61(2–3), 195–205.

He, Y. C., Chan, P. W., and Li, Q. S. (2013). "Wind characteristics over different terrains." *Journal of Wind Engineering and Industrial Aerodynamics*, 120.

Holmes, J. (2007). *Wind Loading on Structures*. Taylor&Francis, New york.

Hu, J., and Ou, J. (2013). "Wind field characteristics analysis at a long-span suspension bridge based on long-term monitoring data." *Zhongnan Daxue Xuebao (Ziran Kexue Ban)/Journal of Central South University (Science and Technology)*, 44(7).

Hu, L., Xu, Y.-L., and Huang, W.-F. (2013). "Typhoon-induced non-stationary buffeting response of long-span bridges in complex terrain." *Engineering Structures*, 57(0), 406–415.

Hu, L., Xu, Y.-L., Zhu, Q., Guo, A., and Kareem, A. (2017). "Tropical Storm–Induced Buffeting Response of Long-Span Bridges: Enhanced Nonstationary Buffeting Force Model." *Journal of Structural Engineering*.

Hui, M. C. H., Larsen, A., and Xiang, H. F. (2009a). "Wind turbulence characteristics study at the Stonecutters Bridge site: Part I-Mean wind and turbulence intensities." *Journal of Wind Engineering and Industrial Aerodynamics*, 97(1), 22–36.

Hui, M. C. H., Larsen, A., and Xiang, H. F. (2009b). "Wind turbulence characteristics study at the Stonecutters Bridge site: Part II: Wind power spectra, integral length scales and coherences." *Journal of Wind Engineering and Industrial Aerodynamics*, 97(1), 48–59.

Ishizaki, H. (1983). "Wind profiles, turbulence intensities and gust factors for design in typhoon-prone regions." *Journal of Wind Engineering and Industrial Aerodynamics*, 13(1–3), 55–66.

Jain, A., Jones, N. P., and Scanlan, R. H. (1996). "Coupled Flutter and Buffeting Analysis of Long-

Span Bridges." *Journal of Structural Engineering*, 122(7), 716–725.

Kaimal, J. C. J., Wyngaard, J. C. J., Izumi, Y., Coté, O. R., and Cote, O. R. (1972). "Spectral Characteristics of Surface-Layer Turbulence." *Quarterly Journal of the …*, 98(417), 563–589.

von Karman, T. (1948). "Progress in the statistical theory of turbulence." *Proceedings of the National Academy of Sciences of the United States of America*, 34(11), 530–539.

Katsuchi, H., Jones, N. P., Scanlan, R. H., and Akiyama, H. (1998). "Multi-mode flutter and buffeting analysis of the Akashi-Kaikyo bridge." *Journal of Wind Engineering and Industrial Aerodynamics*, 77–78, 431–441.

Kimura, K., and Tanaka, H. (1992). "Bridge buffeting due to wind with yaw angles." *Journal of Wind Engineering and Industrial Aerodynamics*, 42(1–3), 1309–1320.

Krayer, W. R., and Marshall, R. D. (1992). "Gust Factors Applied to Hurricane Winds." *Bulletin of the American Meteorological Society*.

Krenk, S. (1996). "Wind Field Coherence And Dynamic Wind Forces." *IUTAM Symposium on Advances in Nonlinear Stochastic Mechanics: Proceedings of the IUTAM Symposium held in Trondheim, Norway, 3--7 July 1995*, A. Naess and S. Krenk, eds., Springer Netherlands, Dordrecht, 269–278.

Kristensen, L., and Jensen, N. O. (1979). "Lateral coherence in isotropic turbulence and in the natural wind." *Boundary-Layer Meteorology*, 17(3), 353–373.

Kristiansen, S., Mamen, J., and Szewczyk-Bartincka, H. (2016). *Weather in Norway: Monthly Climatological Report: January 2016 (in Norwegian)*. Norwegian Meteorological Institute, Oslo.

Kwon, D. K., and Kareem, A. (2014). "Revisiting Gust Averaging Time and Gust Effect Factor in ASCE 7." *Journal of Structural Engineering*, 140(11), 6014004.

Li, L., Kareem, A., Xiao, Y., Song, L., and Zhou, C. (2015). "A comparative study of field measurements of the turbulence characteristics of typhoon and hurricane winds." *Journal of Wind Engineering and Industrial Aerodynamics*, 140.

Macdonald, J. H. G. (2003). "Evaluation of buffeting predictions of a cable-stayed bridge from full-scale measurements." *Journal of Wind Engineering and Industrial Aerodynamics*, 91(12–15), 1465–1483.

Mann, J. (2006). "The spatial structure of neutral atmospheric surface-layer turbulence." *Journal of Fluid Mechanics*, 273(1), 141.

McCullough, M., Kwon, D. K., Kareem, A., and Wang, L. (2014). "Efficacy of averaging interval for nonstationary winds." *Journal of Engineering Mechanics*, 140(1).

Miyata, T., Yamada, H., Katsuchi, H., and Kitagawa, M. (2002). "Full-scale measurement of Akashi-Kaikyo Bridge during typhoon." *Journal of Wind Engineering and Industrial Aerodynamics*, 90(12–15), 1517–1527.

Norwegian Meteoroligical Institute. (2016). *Extreme weather report: Storm Tor 29-30 January 2016*. Oslo.

Øiseth, O., Rönnquist, A., and Sigbjörnsson, R. (2010). "Simplified prediction of wind-induced response and stability limit of slender long-span suspension bridges, based on modified quasi-steady theory: A case study." *Journal of Wind Engineering and Industrial Aerodynamics*, 98(12), 730–741.

Pagnini, L. C., and Solari, G. (2002). "Gust buffeting and turbulence uncertainties." *Journal of Wind Engineering and Industrial Aerodynamics*, 90(4–5), 441–459.

Park, J., Kim, H.-K., Lee, H. S., Koh, H.-M., and Cho, S. (2012). "Buffeting responses of a cable-stayed bridge during the typhoon Kompasu." *Bridge Maintenance, Safety, Management, Resilience and Sustainability*, Bridge Maintenance, Safety and Management, CRC Press, 1158–1161.

Peeters, B., and De Roeck, G. (2001). "Stochastic System Identification for Operational Modal Analysis: A Review." *Journal of Dynamic Systems, Measurement, and Control*, 123(4), 659.

Peng, H., Xu, W., and Ming, G. (2013). "Study on near-ground wind characteristics of a strong typhoon-wind speed, turbulence intensities, gust factors and peak factors." *Disaster Advances*, 6(5).

Petersen, Ø. W., and Øiseth, O. (2017). "Finite element model updating of a long span suspension bridge." *The International Conference on Earthquake engineering and Structural Dynamics, Reykjavik, Iceland*.

Scanlan, R. H. (1978). "The action of flexible bridges under wind, II: Buffeting theory." *Journal of*

Sound and Vibration, 60(2), 187–199.

Scanlan, R. H., and Tomko, J. J. (1971). "Airfoil and Bridges Deck Flutter Derivatives." *Journal of the Engineering Mechanics Division (ASCE)*, 97, 1717–1737.

Shu, Z. R., Li, Q. S., He, Y. C., and Chan, P. W. (2015). "Gust factors for tropical cyclone, monsoon and thunderstorm winds." *Journal of Wind Engineering and Industrial Aerodynamics*, 142, 1–14.

Siedziako, B., Øiseth, O., and Rønnquist, A. (2017). "An enhanced forced vibration rig for wind tunnel testing of bridge deck section models in arbitrary motion." *Journal of Wind Engineering and Industrial Aerodynamics*, 164, 152–163.

Simiu, E., and Scanlan, R. H. (1996). *Winds Effects on Structures: Fundamentals and Applications to Design*. Wiley.

Solari, G., and Piccardo, G. (2001). "Probabilistic 3-D turbulence modeling for gust buffeting of structures." *Probabilistic Engineering Mechanics*, 16(1), 73–86.

Statens-Vegvesen. (2009). *N400 Handbook for bridge design*.

Tao, T., Wang, H., and Wu, T. (2017). "Comparative Study of the Wind Characteristics of a Strong Wind Event Based on Stationary and Nonstationary Models." *Journal of Structural Engineering*, American Society of Civil Engineers, 143(5).

Toriumi, R., Katsuchi, H., and Furuya, N. (2000). "A study on spatial correlation of natural wind." *Journal of Wind Engineering and Industrial Aerodynamics*, 87(2–3), 203–216.

Wang, H., Hu, R., Xie, J., Tong, T., and Li, A. (2013). "Comparative study on buffeting performance of sutong bridge based on design and measured spectrum." *Journal of Bridge Engineering*, 18(7), 587–600.

Wang, H., Li, A., Guo, T., and Xie, J. (2009). "Field measurement on wind characteristic and buffeting response of the Runyang Suspension Bridge during typhoon Matsa." 52(5), 1354–1362.

Wang, H., Li, A., and Hu, R. (2011). "Comparison of Ambient Vibration Response of the Runyang Suspension Bridge under Skew Winds with Time-Domain Numerical Predictions." *Journal of Bridge Engineering*, 16(4), 513.

Wang, H., Wu, T., Tao, T., Li, A., and Kareem, A. (2016). "Measurements and analysis of non-stationary wind characteristics at Sutong Bridge in Typhoon Damrey." *Journal of Wind Engineering and Industrial Aerodynamics*, 151, 100–106.

Wang, X., Chen, B., Sun, D., and Wu, Y. (2014). "Study on typhoon characteristic based on bridge health monitoring system." *Scientific World Journal*, 2014.

Wang, X., Huang, P., Yu, X.-F., Wang, X.-R., and Liu, H.-M. (2017). "Wind characteristics near the ground during typhoon Meari." *Journal of Zhejiang University: Science A*, 18(1).

Welch, P. D. (1967). "The Use of Fast Fourier Transform for the Estimation of Power Spectra: A Method Based on Time Averaging Over Short, Modified Periodograms." *IEEE Transactions on Audio and Electroacoustics*, 15(2), 70–73.

Xie, J., Tanaka, H., Wardlaw, R. L., and Savage, M. G. (1991). "Buffeting analysis of long span bridges to turbulent wind with yaw angle." *Journal of Wind Engineering and Industrial Aerodynamics*, 37(1), 65–77.

Xu, Y.-L. (2013). *Wind Effects on Cable-Supported Bridges*. John Wiley & Sons.

Xu, Y. L., and Chen, J. (2004). "Characterizing nonstationary wind speed using empirical mode decomposition." *Journal of Structural Engineering-Asce*, 130(6), 912–920.

Xu, Y. L., Sun, D. K., Ko, J. M., and Lin, J. H. (2000). "Fully coupled buffeting analysis of Tsing Ma suspension bridge." *Journal of Wind Engineering and Industrial Aerodynamics*, 85(1), 97–117.

Xu, Y. L., and Zhu, L. D. (2005a). "Buffeting response of long-span cable-supported bridges under skew winds. Part 2: Case study." *Journal of Sound and Vibration*, 281(3–5), 675–697.

Xu, Y. L., and Zhu, L. D. (2005b). "Buffeting response of long-span cable-supported bridges under skew winds. Part 2: case study." *Journal of Sound and Vibration*, Academic Press, 281(3–5), 675–697.

Xu, Y. L., Zhu, L. D., Wong, K. Y., and Chan, K. W. Y. (2001). "Field measurement results of Tsing Ma suspension bridge during typhoon Victor." *Structural Engineering and Mechanics*, 10(6), 545–559.

Xu, Y. L., Zhu, L. D., and Xiang, H. F. (2003). "Buffeting response of long suspension bridges to skew winds." *Wind and Structures, An International Journal*, 6(3), 179–196.

Zhu, L. D., and Xu, Y. L. (2005). "Buffeting response of long-span cable-supported bridges under skew winds . Part 1 : theory.” *Journal of Sound and Vibration*, 281(3–5), 647–673.